

Development of ANCF Airless Tire Model for the Mars Rover

BY

EDOARDO SAMARINI
B.S., Politecnico di Torino, Turin, Italy, 2018

THESIS

Submitted as partial fulfillment of the requirements
for the degree of Master of Science in Mechanical Engineering
in the Graduate College of the
University of Illinois at Chicago, 2020

Chicago, Illinois

Defense Committee:

Ahmed A. Shabana, Chair and Advisor
Emanuele Grossi
Aurelio Somà, Politecnico di Torino

ACKNOWLEDGMENTS

Firstly, I would like to thank my thesis committee for the continuous support of my master study, for their patience, motivation, and immense knowledge. Their insightful comments, encouragement, and hard questions incited me to extend my research from various perspectives. I thank all my friends from university for the stimulating discussions, for the sleepless nights we were working together before deadlines, and for all the fun we have had in the last years.

Last but not the least, I would like to thank my family for supporting me throughout my life in general. A heartfelt thanks goes to my mum Monica who has made this all possible. She has been a constant source of support and encouragement and has made an untold number of sacrifices for the entire family, and specifically for me to continue my schooling. She is a great inspiration to me. This thesis is dedicated to the memory of my father and to my mother with love and eternal appreciation. I thank you all.

ES

CONTRIBUTIONS OF AUTHORS

My advisor, Dr. Ahmed A. Shabana, contributed to the development of the formulation used, provided the software used in the computer simulations and, together with Dr. Emanuele Grossi, supervised the research, reviewed and edited the thesis to be completed based on this research.

TABLE OF CONTENTS

<u>CHAPTER</u>		<u>PAGE</u>
1	INTRODUCTION.....	1
1.1	Background, Scope and Contributions of this Investigation	3
1.2	Discrete and Continuum-Based Tire Models.....	5
1.3	Scope of this Investigation.....	5
1.4	Contributions of this Investigation.....	7
1.5	Thesis Structure	9
2	GEOMETRY/ANALYSIS APPORACH.....	11
2.1	MBS Algorithms.....	11
2.2	Rover Structure	12
2.3	Continuum-Based Airless Tires	14
2.3.1	Airless-Tire Geometry and Mars Terrain	14
2.3.2	Absolute Nodal Coordinate Formulation (ANCF).....	17
2.3.3	Unified ANCF Geometry/Analysis Mesh	19
2.3.4	Structural Discontinuities	24
2.3.5	Airless-Tire Assembly.....	26
2.4	Traction and Tire Contact Forces	28
2.4.1	Tire Contact Algorithm	28
2.4.3	Tractive Forces	30
2.5	Geometry/Analysis Integration.....	32
2.5.1	Reference-Configuration Geometry and Elastic Forces.....	33
2.5.2	Constrained Dynamic Equations	34
2.5.3	Computational Considerations	35
3	NUMERICAL RESULTS.....	36
3.1	Rover Model Description.....	36
3.2	Brush-Type Rover Model	40
3.3	ANCF Airless Tires	45
3.4	Comparative Study.....	47

TABLE OF CONTENTS (continued)

3.5 Tractive Force 50

4 SUMMARY AND CONCLUSIONS 52

CITED LITERATURE 53

VITA..... 60

LIST OF TABLES

<u>TABLE</u>		<u>PAGE</u>
I	ROVER INERTIA PROPERTIES	37
II	BRUSH-TYPE TIRE PARAMETERS	44

LIST OF FIGURES

<u>FIGURE</u>		<u>PAGE</u>
1	Mars rover.....	3
2	Airless tire.....	4
3	Brush and ANCF tire models.....	6
4	Bogie electro-mechanical assembly (BEMA) subsystem.....	12
5	Different actuator positions.....	13
6	Wheel details.....	15
7	Deformation-force curves (Sivo et al., 2019).....	16
8	Airless tire mesh developed using ANCF fully parameterized plate elements	20
9	Three geometry configurations.....	22
10	Airless-tire structural discontinuities.....	24
11	ANCF reference node.....	28
12	Contact forces.....	30
13	Components of the rover.....	37
14	Rover revolute joints.....	38
15	Weight distribution on the rover wheels.....	39
16	Rover model with the brush-type tires.....	40
17	Average stiffness curve (Sivo at al., 2019).....	41
18	Vertical force on a brush-type tire in the free fall scenario.....	42
19	Deformation of a brush-type tire in the free fall scenario.....	43
20	Verification of the brush-type tire model.....	45
21	Rover model with ANCF airless tires.....	46
22	Verification of the ANCF airless tire.....	47
23	Forward velocity of the principal body.....	48
24	Comparison between brush-type and ANCF airless tires.....	50
25	Tractive force.....	51

LIST OF ABBREVIATION

MBS	Multibody system
ANCF	Absolute Nodal Coordinate Formulation
DAE	Differential/Algebraic Equation
FE	Finite Element
CAD	Computer-Aided-Design
B-Splines	Basis Splines
NURBS	Non-Uniform Rational B-Splines
BEMA	Bogie Electro-Mechanical Assembly
DRV	Drive
STR	Steering
DEP	Deployment
I-CAD-A	Integration of Computer-Aided-Design and Analysis
RBE	Rigid-Body Element
ANCF-RN	Absolute Nodal Coordinate Formulation Reference Node
Sigma/Sams	Systematic Integration of Geometric Modeling and Analysis for the Simulation of Articulated Mechanical Systems
CAE	Computer-Aided Engineering
NVH	Noise, Vibration and Harshness

SUMMARY

Because of the scientific challenges of space explorations, several space agencies are involved in the design of autonomous planetary surface exploration devices. Examples are *Mars rovers*, designed with the goal of collecting terrain information, including dust, soil, rocks, and liquids. The design of such sophisticated rovers can be enhanced by less reliance on trial-and-error process, building expensive physical models, and time-consuming experimental testing. Physics-based virtual prototyping is necessary for an efficient and credible Mars rover designs. In this thesis, a new flexible multibody system (MBS) rover model for planetary exploration is developed. Because the rover, a *wheeled robot*, must be designed to negotiate uneven terrains, the *airless wheels* must be able to adapt to different soil patterns and harsh operating and environmental conditions. In order to describe accurately the airless-wheel complex geometry and capture its large deformations and rotations, the *absolute nodal coordinate formulation* (ANCF) finite elements are used. A numerical study is performed to compare the ANCF kinematics and tractive force results with the results of the discrete brush tire model, widely used in the vehicle-dynamics literature. Several simulation scenarios are considered, including a drop test and acceleration along a straight line. The numerical results obtained are verified using data published in the literature and are used to evaluate the accuracy and computational efficiency of the ANCF airless-tire modeling approach.

CHAPTER 1

INTRODUCTION

Space exploration missions aimed at finding different forms of life elsewhere in the universe are one of the most ambitious scientific challenges. This is particularly true in the case of the exploration of Mars, which has the potential of providing biological signatures because of its past geological history. Future Mars space missions aim at searching for proof of life by analyzing soil samples collected by a drill, directly mounted on wheeled rovers that function as robots. The wheeled-robots must be capable of negotiating rocky and uneven terrains that characterize the Mars planet. Consequently, accurate prediction of the kinematic and dynamic responses of the rover is critical for robust design, credible validation and verification, and science-based planning of such sophisticated machines. An important aspect that must be considered is the dynamic interaction between the soil and the rover wheels, which transmit the loads from the uneven and rocky terrain to other components of the wheeled robot.

Mars is the fourth planet in the solar system and has been recognized as the first candidate among other solar planets for space exploratory missions. The distance between the Earth and Mars varies depending on their orbital location; with an average distance of 225 million km. Because the two planets can be 401 million km apart, Mars rover launch missions are planned to take advantage of the closest relative position of the two planets. Mars extreme environmental conditions can potentially cause damage to mechanical devices, equipment, and machines. Among these conditions are the high-velocity dusty winds, low gravity, ultraviolet radiation, and significant daily variation in temperature and atmospheric pressure. The average of the wind velocity is 20 m/s and can rise to peaks of 25 m/s during dust storms. The atmospheric pressure,

depending on the season, altitude and weather, varies from 7 to 9 mbar . Similarly, surface temperatures can vary widely between $-143\text{ }^{\circ}\text{C}$ and $35\text{ }^{\circ}\text{C}$; with the possibility of daily temperature variation in the range of $50\text{ }^{\circ}\text{C}$. In general, Mars has a lower average temperature than the Earth because of its larger distance from the sun. Because of the Mars extreme environmental conditions and the Mars uneven and rocky terrain, the rover design has to be robust and reliable and must ensure successful completion of the scientific exploratory missions.

Regions of Mars which attract the highest scientific interest are characterized by very rough terrains. Mars poles, on the other hand, represent safer soil, despite the fact that the temperature could sink to $-125\text{ }^{\circ}\text{C}$. At this temperature level, martensitic steels become brittle, potentially causing failure of robot components made of this material, particularly when subjected to impacts or cyclic fatigue. Thermal stresses, resulting from high temperature variations during one day, can easily cause damage to the rover components. Furthermore, while negotiating uneven terrains might falsely appear easier because of the lower gravity of the planet, 3.711 m/s^2 as compared to the earth 9.81 m/s^2 , one must keep in mind that such low gravity can result in loss of traction and inefficiencies in propelling forward the wheeled robot. Due to repeated high impulsive forces resulting from component-surface impacts, a dust storm can instantaneously damage and/or corrode the materials of the wheeled robot. Mechanical joints of the rover are particularly susceptible to malfunction because of dust, small particles, and debris that enter between jointed components, causing corrosion and abrasive wear, which can lead to joint failure.

In order to successfully complete space missions, the Mars rover is designed to satisfy several requirements (Poulakis et al., 2015). Among these requirements are the ability to collect samples between two points up to two kilometers apart; ability to cross the rough Martian terrain with a range of rock distributions; lateral and longitudinal gradeability of slopes up to 25° ; ability to

overcome obstacles up to 0.25 m height and cross crevasses with length of 0.15 m ; ability to move at an average locomotion speed of 70 m/h ; point-turn capability; and static stability of at least 40° in all directions.

1.1 Background, Scope and Contributions of this Investigation

Figure 1 shows an image of the Mars rover model considered in this investigation. This wheeled robot interacts with the Mars uneven terrain using airless tires, which provide support and serve as a vibration-isolation system.

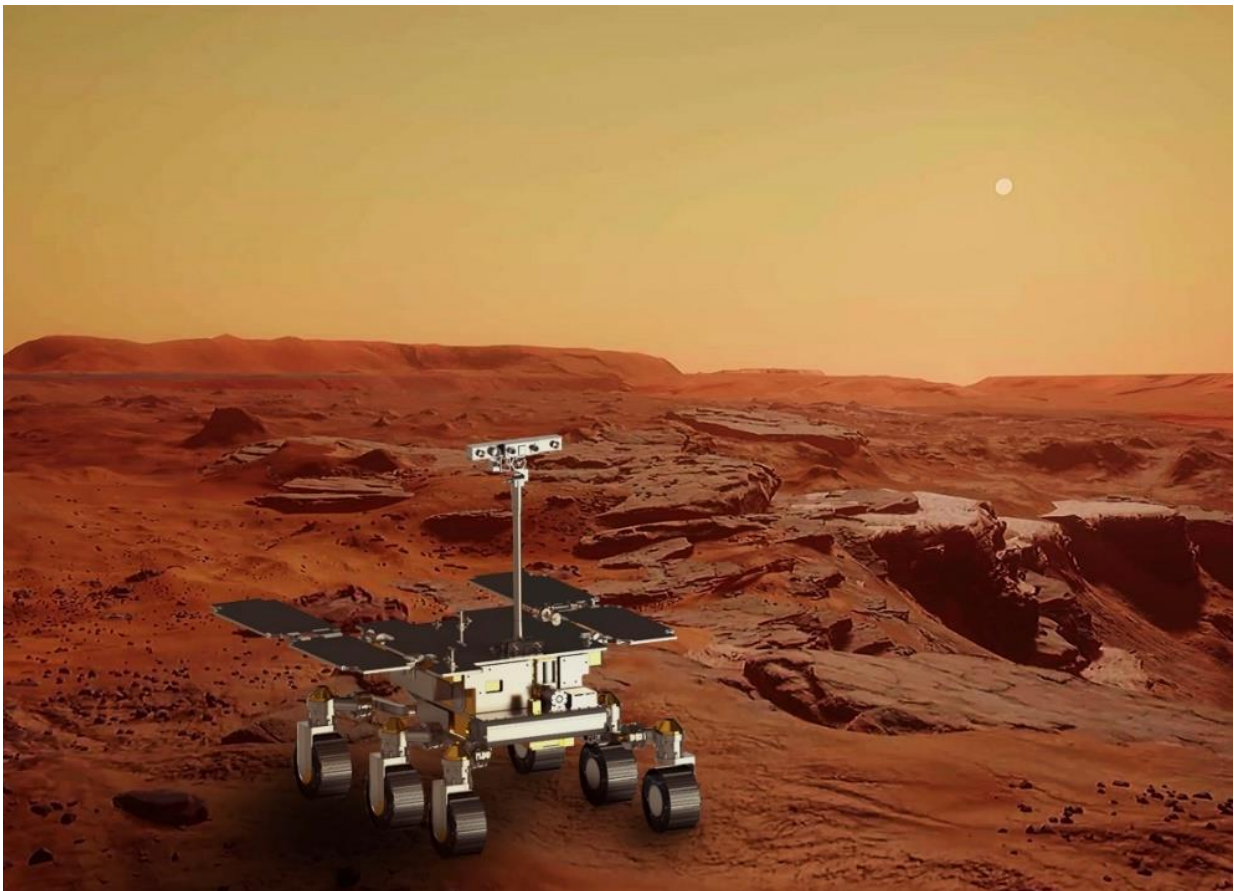


Figure 1. Mars rover

Because the wheeled robot does not have suspension springs, the airless tires play an important role in defining the kinematic and dynamic characteristics of the rover. Airless tires, such as the ones shown in Fig. 2, are used because of their high durability that gives them an advantage over pneumatic tires that are prone to punctures that can disable the rover and terminate its exploratory mission. Therefore, the design and integrity of the airless tires are critical in ensuring successful completion of the rover mission.

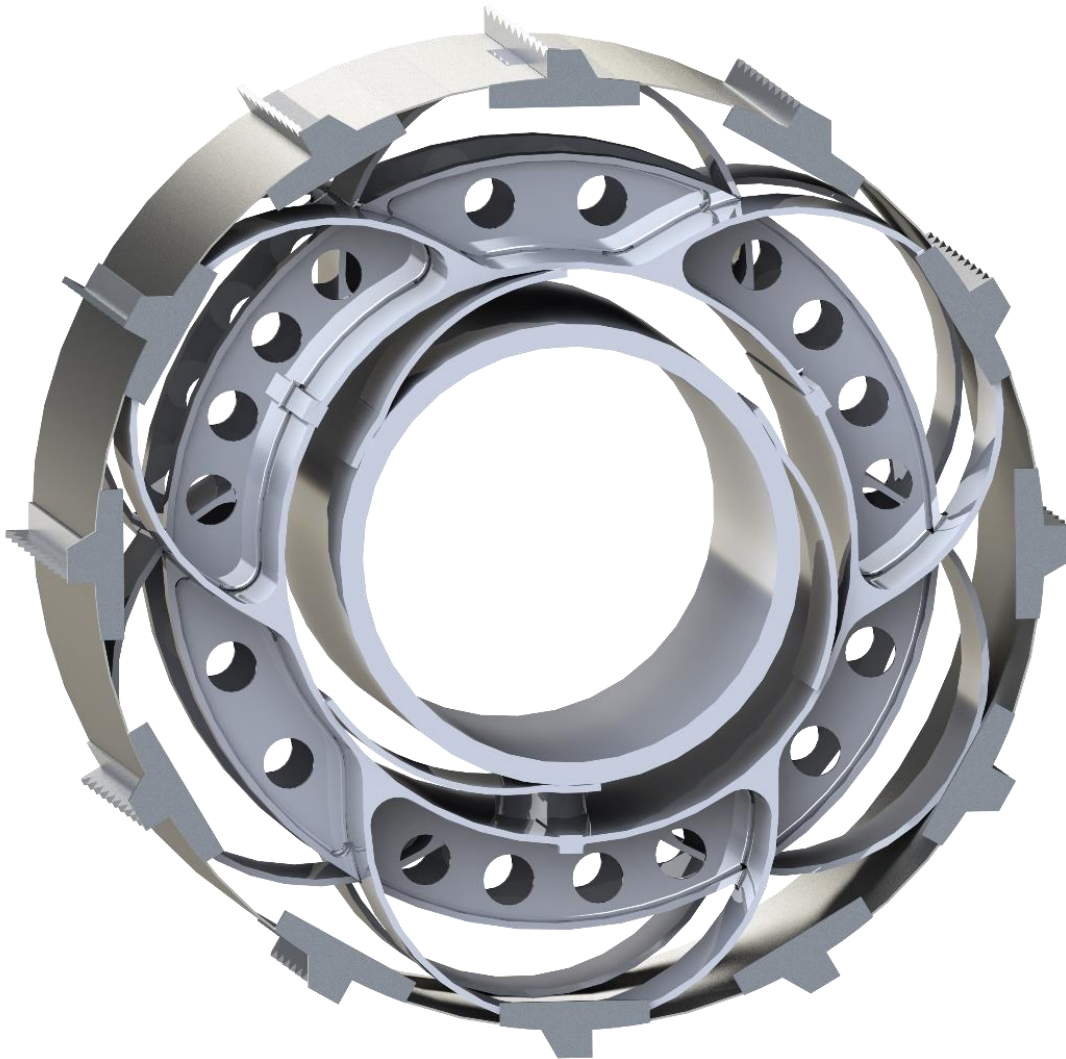


Figure 2. Airless tire

1.2 Discrete and Continuum-Based Tire Models

Simple discrete tire models may be adequate in investigations focused on the effect of the terrain inputs on the vehicle dynamics. However, such discrete simple models, which are often developed using spring-damper systems, are not adequate to study the tire integrity and durability and do not correctly capture the high frequency variations in the tire/terrain contact forces. While the discrete spring-damper models that produce discrete forces have been used in the literature to examine the motion of vehicles in response to terrain variations under different operating conditions, such simple models do not account for the tire distributed elasticity and inertia, do not allow predicting strain distributions, cannot be used to accurately determine the tire distributed stresses and wear, and cannot be used to accurately describe and account for the complex tire geometry particularly in the case of airless tires. Continuum-based tire formulations become necessary if these limitations are to be avoided. Such continuum-based tire formulations are also necessary for systematically accounting for the Mars extreme environmental conditions including the significant temperature variations. Another important design consideration is the accurate prediction of the *tractive forces* in the Mars low gravity environment. Use of continuum-based tires also leads to a more realistic, larger, and conformal contact area as compared to the discrete tire models.

1.3 Scope of this Investigation

Accounting for the airless-tire distributed inertia and elasticity is essential for developing high-fidelity *multibody system* (MBS) rover models. In this investigation, the *absolute nodal coordinate formulation* (ANCF) is used to develop both the *geometry* and *analysis meshes* (Hu et al., 2014; Fotland et al., 2019; Nachbagauer, 2014; Orzechowski and Fraczek, 2015; Shen et al., 2014; Ma et al., 2016; Ma et al., 2020; Obrezko et al., 2020; Liu et al., 2011; Shabana, 2018; Pappalardo et

al., 2020; Wang, 2020). Constant mass matrix and zero Coriolis and centrifugal inertia forces are some of the various desirable features of the ANCF elements. In this study, the airless tires are modeled using fully parametrized ANCF plate elements, which allow for describing accurately the tire geometry. In addition to using the continuum-based ANCF tire formulation, a discrete brush-type tire model that consists of rigid bodies connected by springs and dampers is used for the purpose of comparison and verification (Gipser, 2005; Lugner et al., 2005; Pacejka, 2006). However, this simpler discrete tire modeling approach, as previously mentioned, fails to capture geometric details as well as geometric and material nonlinearities that cannot be ignored in the planning of critical and costly space missions. The second approach is based on the ANCF *geometry/analysis method* which allows alleviating the limitations of the discrete tire models. The two different tire models considered in this study are shown in Fig. 3.

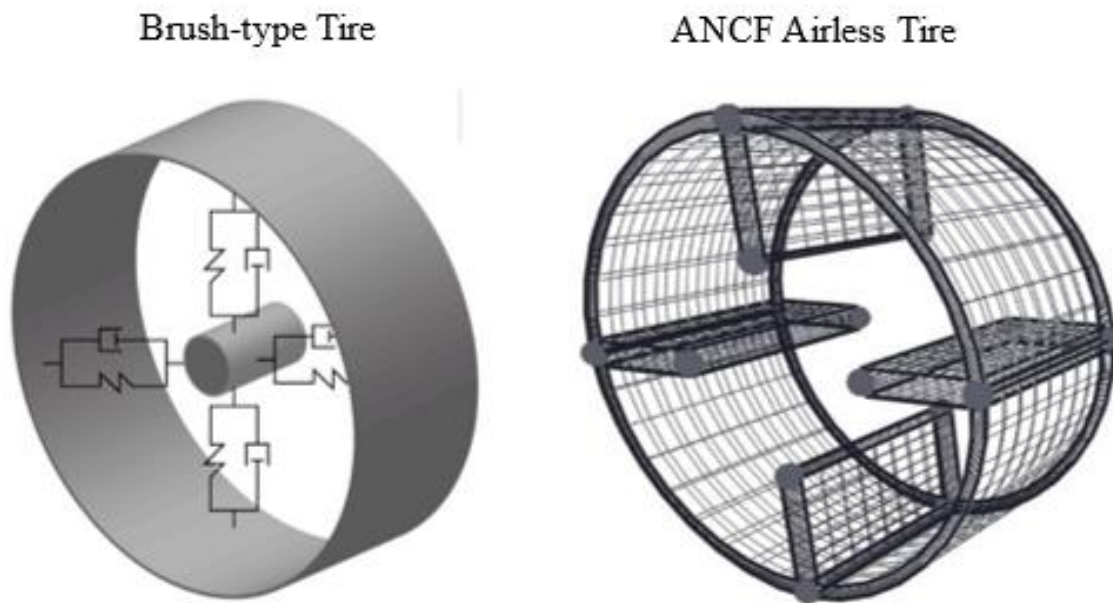


Figure 3. Brush and ANCF tire models

The ANCF tire formulation was previously used in the literature to develop physics-based tire models (Patel et al., 2016; Pappalardo et al., 2017; He et al., 2017; Grossi et al., 2019). An ANCF wheel model for Mars exploration rover was recently proposed by Sivo et al. (2019), who developed a detailed FE wheel mesh and performed a nonlinear static analysis in order to characterize the wheel stiffness properties. In the work of Sivo et al., however, no MBS model for the Mars rover was developed, and their study was focused mainly on the stiffness characterization of the tire.

The goal of this investigation is to develop a new Mars rover MBS virtual prototyping model that includes tires with distributed inertia and elasticity. The model developed in this study is verified using results previously published in the literature, including some of the results reported by Sivo et al. (2019). The newly developed MBS dynamic rover model allows predicting the tire deformations, can be used in different motion scenarios, can be integrated with general MBS algorithms that systematically construct and numerically solve the rover differential/algebraic equations (DAEs), and can be generalized in future investigations to study the effect of the Mars environmental conditions including the effect of the significant temperature variations.

1.4 Contributions of this Investigation

Airless wheels are often used for space robots in order to avoid serious problems and rover malfunction that can result from using pneumatic tires, which are prone to puncturing and are less durable in harsh environmental conditions. Nonetheless, airless wheels often have complex geometries that make their virtual analysis and integration with virtual rover MBS models more challenging. Conventional finite element (FE) formulations have well-known limitations in the analysis of tires and other soft components with complex geometries. Recent investigations have demonstrated that conventional FE formulations do not lead to accurate results in case of large

displacements of soft and fluid materials (Ma et al., 2020; Obrezko, 2020; Shabana and Zhang, 2020). This lack of accuracy is attributed to the conventional FE kinematics and to adopting the co-rotational solution procedure widely used in commercial FE software. Furthermore, such conventional FE formulations are not related by a linear mapping to the computational geometry methods used in the **computer-aided-design** (CAD) software. In the CAD software, **Basis Splines** (B-splines) and **Non-Uniform Rational B-Splines** (NURBS) are used to develop the solid-model geometry (Piegl and Tiller, 1997; Farin, 2003; Rogers, 2001; Gallier, 2011; Goetz, 1970; Kreyszig, 1991). The airless tires of space wheeled-robots have complex geometry and are subjected to environmental and operating conditions that necessitate use of geometrically-accurate formulations capable of capturing large rotational motion as well as large deformations. These formulations must also allow for systematic integration of the airless-tire meshes with computational MBS algorithms designed to solve the governing DAEs of the wheeled robot.

In this study, a new computational approach is used for the nonlinear analysis of the Mars rover system. The new approach allows developing detailed flexible MBS rover models that include continuum-based airless tires. In the proposed computational framework, ANCF fully-parameterized plate elements are used to develop a unified tire *geometry/analysis mesh*. The main contributions of this study can be summarized as follows:

1. A new detailed MBS rover model with airless tires, that have distributed inertia and elasticity, is developed and integrated with a computational MBS algorithm designed to systematically construct and numerically solve the system DAEs.
2. The rover-tire geometry and analysis mesh is developed using ANCF fully-parameterized plate elements that take into account structural discontinuities. This feature is important in the definition of the geometry of the airless tires.

3. The concept of the ANCF reference node is used to assemble the six tires of the rover at a preprocessing stage. That is, all the rover tires at the geometry and analysis stages are represented by one FE mesh despite the fact that these tires can have arbitrarily large displacements, including finite rotations, with respect to each other.
4. An approach for the prediction of the *tractive forces* of the airless-tire rover is outlined in this study. The contact forces are evaluated by defining a point mesh on the ANCF plate elements. This point mesh is used to determine the tire/terrain contact patch leading to a more realistic representation of the contact geometry and tractive forces. The results obtained in this study show that the continuum-based tire model can capture the oscillations in the airless-tire tangential friction forces.
5. Using the nonlinear MBS approach adopted in this investigation, a study is performed to compare between rover models developed using the discrete brush-type and continuum-based ANCF tire models. The results obtained in this investigation are verified by comparing with numerical data published in the literature. The advantages and limitations of each tire model are discussed.

1.5 Thesis Structure

This thesis is organized as follows. Chapter 2 discusses the main features of the Mars rover used in this investigation and explains its main components that make the rover function as a wheeled robot. It continuously describes the continuum-based ANCF tire used in this study and explains wheel-design issues that are considered for the Mars-exploration vehicle. The ANCF large-deformation analysis, ANCF treatment of structural discontinuities, and ANCF concept of the *reference node* are among the topics discussed. The traction and tire contact force models are then discussed, describing the displacement field of the fully-parameterized ANCF finite element

used in this investigation. The form of the constrained dynamic equations of motion used in the computational algorithm employed to solve the rover equations is presented also. Chapter 3 presents the two rover models developed in this investigation; the discrete brush-type tire model and the continuum-based ANCF airless tire model. After verification of the results by comparing with the results available in the literature, nonlinear dynamic simulations of the rover are performed and the results of different models are compared. Chapter 4 presents summary and conclusions of the study.

CHAPTER 2

GEOMETRY/ANALYSIS APPROACH

In order to avoid the costly and time-consuming process of building physical prototypes which cannot be used to conveniently experiment with design modifications, *virtual prototyping* is becoming the preferred approach for developing the initial designs. Virtual prototyping allows for easily experimenting with different design parameters and configurations and can be used to significantly reduce reliance on physical prototyping and experimentation.

2.1 MBS Algorithms

MBS algorithms, in particular, play a significant role in the design of physics and engineering systems that consist of interconnected bodies that experience arbitrarily large relative displacements and rotations. While it is difficult to reproduce the Martian environmental conditions on Earth when heavily relying on physical prototyping, virtual prototyping allows changing the environmental conditions over a wide parameter range without the need for extensive, costly, and error-prone experimentation. For these reasons, the initial design, testing, and planning of a Mars wheeled-robot are currently being made by first developing and analyzing reliable and accurate physics-based virtual models using *MBS algorithms*. These algorithms allow developing detailed models that include interconnected rigid and flexible bodies, for performing computer simulations for different motion scenarios and operating and loading conditions, and for studying the interaction between the tires and soil. Among the main concerns in the design of Mars wheeled-robots are the static stability of the vehicle over steep slopes and the ability to negotiate a terrain characterized by rocks and crevasses. With regard to the terrain unevenness and discontinuities, practicing engineers and researchers worked on the design of certain types of tires that can

experience large deformations to provide the flexibility needed for successfully negotiating terrains with different irregularities, discontinuities, and material properties. The goal is to achieve higher degree of mobility and obtain the desired performance when the robot negotiates both soft soils (sands, fine granular materials) and rigid surfaces (rocks, coarse granular materials). The development of a reliable and efficient MBS rover model, which is among the goals of this study, represents one of the first steps in planning a Mars space mission. The conclusions based on the numerical results of the virtual experimentation with the MBS model can provide valuable information and can serve as a guide in the design of the wheeled robot as well as in the space mission planning.

2.2 Rover Structure

The Mars rover considered in this investigation is a 6-wheel triple-bogie vehicle, as shown in Fig. 1. The model includes the principal body, on which the drill, sensing, and control equipment are mounted. The system is designed to be autonomously controlled with bogie electro-mechanical assembly (BEMA), which provides the desired mobility as illustrated in Fig. 4.

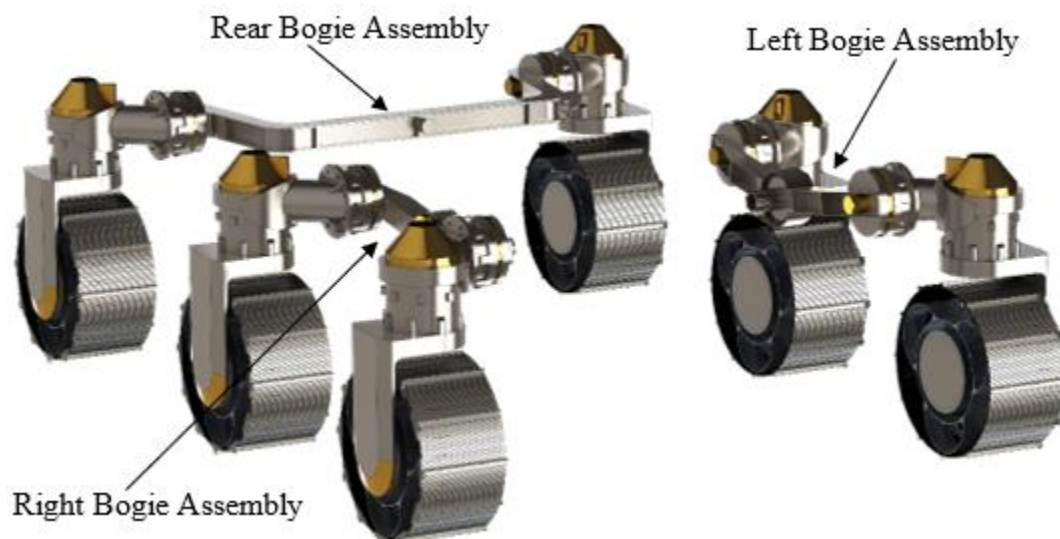


Figure 4. Bogie electro-mechanical assembly (BEMA) subsystem

The BEMA $6 \times 6 \times 6 + 6$ locomotion formula provides good stability of the overall rover when negotiating different rough terrains. This formula, which gives a clear picture of the vehicle topology, implies 6-supporting wheels, 6-driven wheels, 6-steered wheels, plus 6-deployment drivers. Each bogie structure consists of two metallic wheels and eighteen actuators (six *drive* (DRV), six *steering* (STR), and six *deployment* (DEP)), as shown in Fig. 5.

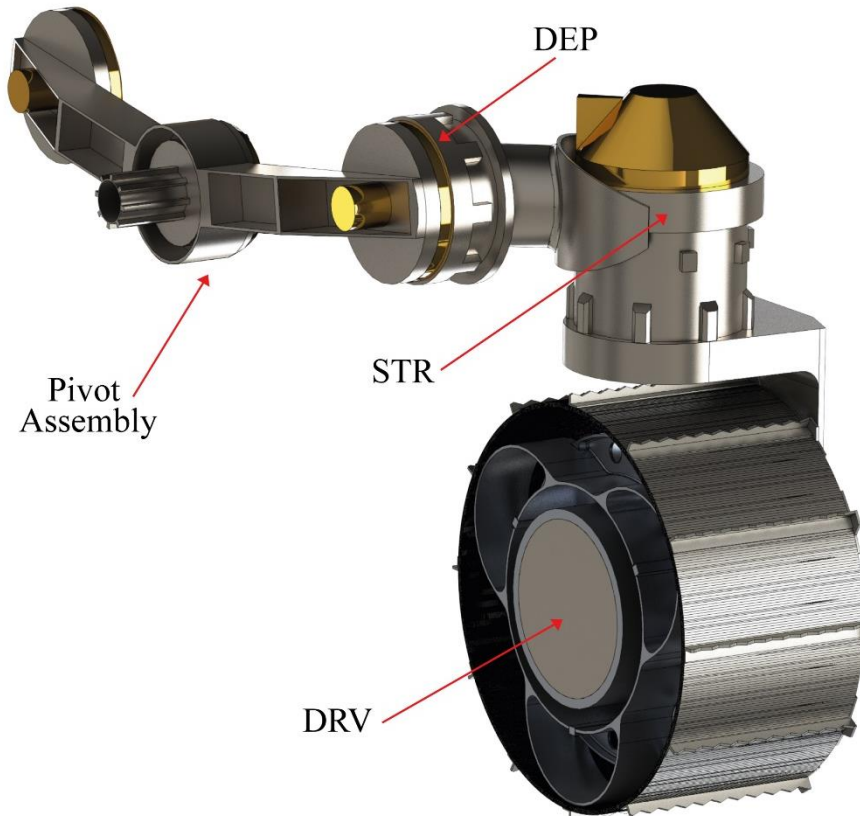


Figure 5. Different actuator positions

The suspension and locomotion elements are designed as thin-walled, riveted box structures made of titanium alloy, in order to maximize the stiffness and minimize the mass. The mobility subsystem is composed of six identical motor modules, placed symmetrically with respect to the

center of mass. These units allow performing drive and turn-on spot maneuvers, as well as powering the vehicle to drive along different terrains and climb over rocks. Each module is equipped with three different independent motors that can be actuated autonomously in order to steer, control the pitch angle, and/or provide the power required for moving the rover wheels over different terrains.

2.3 Continuum-Based Airless Tires

In space wheeled-robots, airless tires are used for their proven durability and for avoiding pneumatic-tire punctures that can result in early termination of costly space missions. Nonetheless, virtual-prototyping investigations of airless tires have been limited because of their complex geometries that need to be modeled accurately and because of the need for an analysis approach that allows capturing accurately the tire large deformations. In this study, a unified airless-tire geometry/analysis mesh is developed and used in the computer simulations of the MBS wheeled-robot model. Such a model demonstrates the value of the integration of computer-aided design and analysis (I-CAD-A) in developing detailed virtual prototyping models for space applications and in avoiding costly conversion of CAD solid models to analysis meshes (Shabana, 2019; Pappalardo et al., 2020).

2.3.1 Airless-Tire Geometry and Mars Terrain

The surface of Mars can be extremely irregular because of crevasses and different types of rocks that cover the soil. Consequently, the robot wheels must be able to adapt and deform in a manner that allows the rover to successfully negotiate obstacles which can have different and irregular shapes. This essential feature plays a key role in the overall rover stability and ability to safely travel over rough terrains.

Several studies have been focused on the design of various types of wheels with the goal of

increasing the soil-contact patch for better force distribution, decreasing the ground pressure to reduce the contact stresses and minimize wear, and providing impact-load absorption capability to avoid severe and unwanted vibrations (Knuth et al., 2012; Johnson et al., 2015). The wheel geometry considered in this study is similar to the geometry proposed by Sivo et al. (2019). Figure 6 shows the principal components of this complex structure, which can be divided into *external tire*, *outer hub*, and *inner hub*. The external tire, in which twelve *grousers* spaced at 30° are installed for enhancing traction capability, is connected to the outer hub by nine operational springs. These springs are divided into six outer springs and three inner springs, mounted out of phase in order to reduce the radial stiffness variation. The outer hub is connected to the inner hub through a cone and impact springs, allowing for relative rotation and displacement between the two hubs.

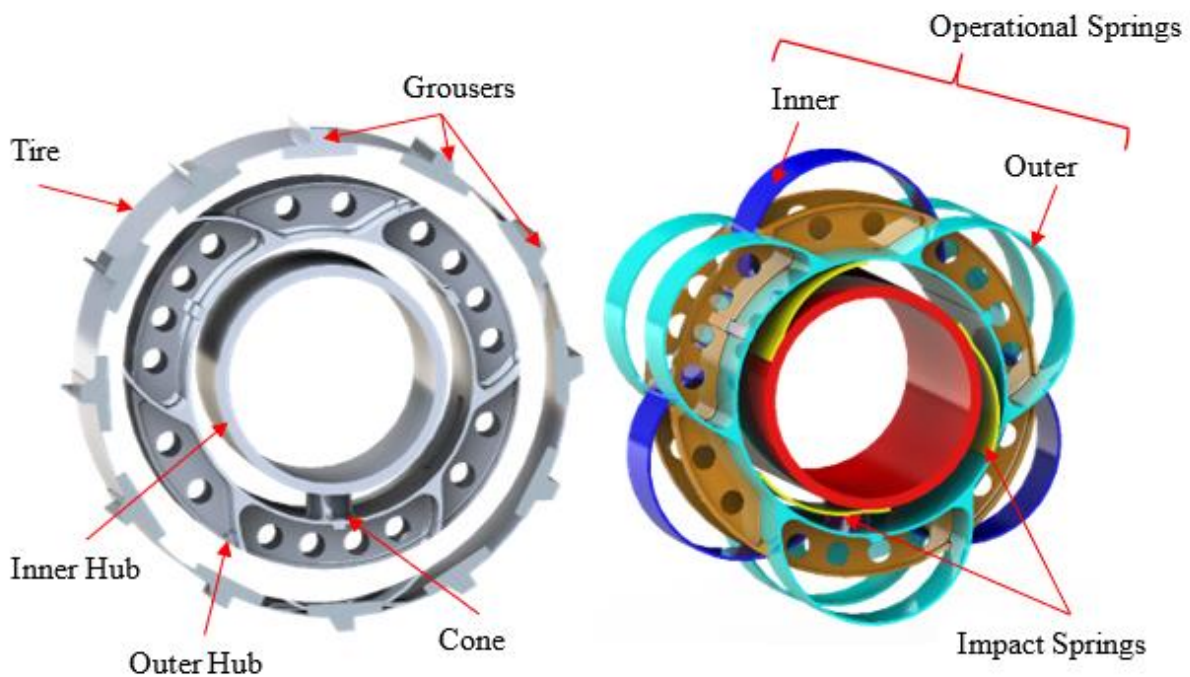


Figure 6. Wheel details

For the purpose of verification of the wheel model developed in this study, the displacement-force curve obtained by Sivo et al. (2019) and shown in Fig. 7 is used. The different curves in this figure, obtained using nonlinear static analysis, represent the stiffness characteristics of the wheel at different circumferential positions.

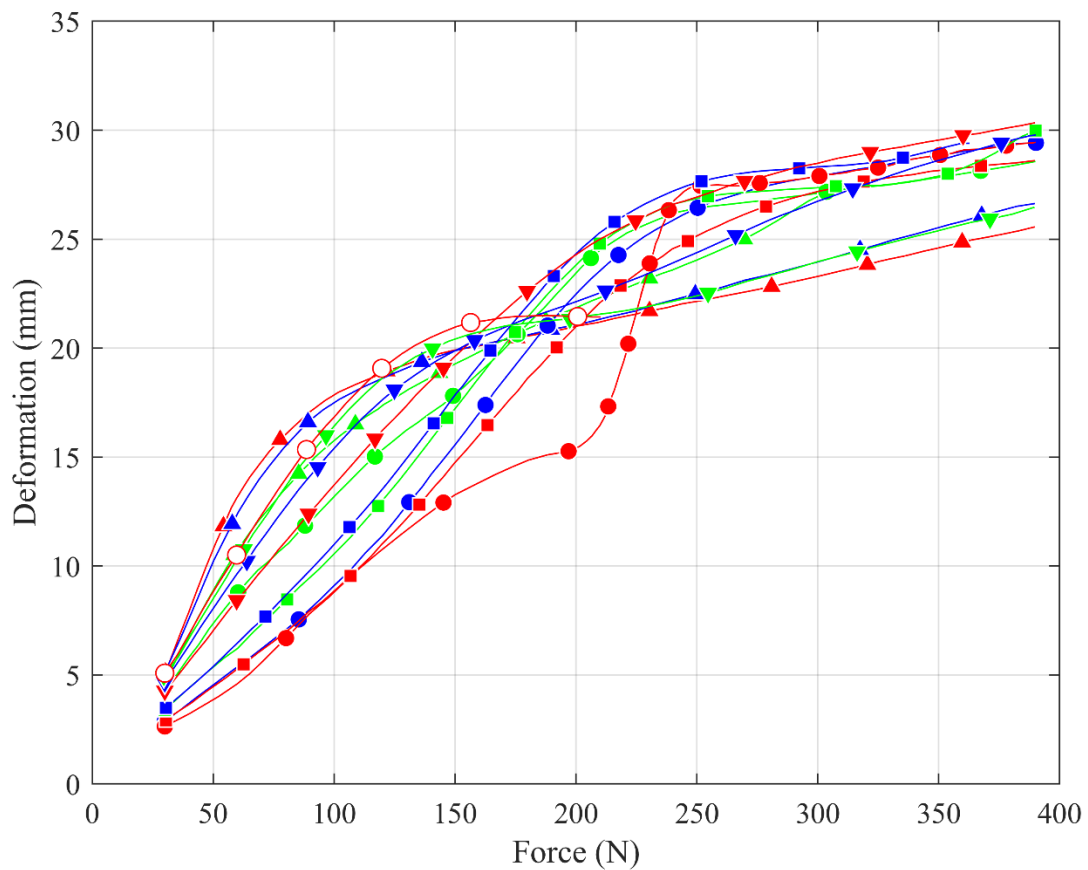


Figure 7. Deformation-force curves (Sivo et al., 2019)

(Wheel circumferential orientation: —▲— 0°, —▲— 5°, —▲— 10°, —●— 15°,
 —●— 25°, —●— 30°, —■— 35°, —■— 40°, —■— 100°, —▼— 105°,
 —▼— 110°, —▼— 115°, —○— 120°)

2.3.2 Absolute Nodal Coordinate Formulation (ANCF)

When the spatial domain of a body is discretized in several different parts, the finite elements are defined as small regions that are connected through different nodal points. The *absolute nodal coordinate formulation* is a finite element method that imposes no limitation on the amount of rotation or deformation within the finite element. In this investigation, ANCF formulation was chosen for its consistency with the non-linear theory of continuum mechanics and for its simplicity that leads to several advantages as compared to other finite element methods. In order to use this formulation, consistent mass formulation must be used for studying the dynamic problem. In addition, to ensure continuity of rotation parameters, the nodal coordinates are defined with global gradients computed with the differentiation of the absolute position vectors with respect to the spatial coordinates.

The displacement of the general element is described by a lower order polynomial because the deformation within the element is in general less lower with respect to the deformation of the body. The body equations of motion are defined assembling all the equations of motion of the elements, thanks to the connectivity conditions at the boundaries. The displacement field for each element is assumed to be:

$$r_k = \begin{bmatrix} 1 & x_1 & x_2 & x_3 & x_1^2 & x_2^2 & \dots \end{bmatrix} \begin{bmatrix} a_{0k} \\ a_{1k} \\ a_{2k} \\ a_{3k} \\ a_{4k} \\ a_{5k} \\ \vdots \end{bmatrix}, \quad k = 1, 2, 3 \quad (2.1)$$

in which $\mathbf{x}^j = [\mathbf{x}_1^j \quad \mathbf{x}_2^j \quad \mathbf{x}_3^j]^T$ is the vector of the spatial coordinates and a_{ik} , $i = 0, 1, 2, 3 \dots$, is a vector of time-dependent coordinates. The preceding equation could be also written as:

$$r_k = \mathbf{P}_k(\mathbf{x})\mathbf{a}_k(t), \quad k=1,2,3 \quad (2.2)$$

where,

$$\mathbf{P}_k(\mathbf{x}) = [1 \quad x_1 \quad x_2 \quad x_3 \quad x_1^2 \quad x_2^2 \quad \dots], \quad \mathbf{a}_k(t) = \begin{bmatrix} a_{0k} \\ a_{1k} \\ a_{2k} \\ a_{3k} \\ a_{4k} \\ a_{5k} \\ \vdots \end{bmatrix}, \quad k=1,2,3 \quad (2.3)$$

The vector of coordinates $\mathbf{e}(t)$ defined at known local points on the element, could be obtained from the Equation 2.2 as:

$$\mathbf{e}(t) = \mathbf{B}_p \mathbf{a}(t) \quad (2.4)$$

where \mathbf{B}_p is a constant square nonsingular matrix and $\mathbf{a}(t)$ is the total vector of the polynomial coefficients. In order to find the different coefficients $\mathbf{a}(t)$, it could be computed $\mathbf{a}(t) = \mathbf{B}_p^{-1} \mathbf{e}(t)$.

In this way the displacement field in terms of the selected coordinates could be written in terms of:

$$\begin{aligned} \mathbf{r}(\mathbf{x}, t) &= \begin{bmatrix} r_1 \\ r_2 \\ r_3 \end{bmatrix} = \begin{bmatrix} \mathbf{P}_1 \mathbf{a}_1 \\ \mathbf{P}_2 \mathbf{a}_2 \\ \mathbf{P}_3 \mathbf{a}_3 \end{bmatrix} = \begin{bmatrix} \mathbf{P}_1 & \mathbf{0} & \mathbf{0} \\ \mathbf{0} & \mathbf{P}_2 & \mathbf{0} \\ \mathbf{0} & \mathbf{0} & \mathbf{P}_3 \end{bmatrix} \begin{bmatrix} \mathbf{a}_1 \\ \mathbf{a}_2 \\ \mathbf{a}_3 \end{bmatrix} \\ &= \mathbf{P}(\mathbf{x}) \mathbf{a}(t) = \mathbf{P}(\mathbf{x}) \mathbf{B}_p^{-1} \mathbf{e}(t) \end{aligned} \quad (2.5)$$

where,

$$\mathbf{P}(\mathbf{x}) = \begin{bmatrix} \mathbf{P}_1 & \mathbf{0} & \mathbf{0} \\ \mathbf{0} & \mathbf{P}_2 & \mathbf{0} \\ \mathbf{0} & \mathbf{0} & \mathbf{P}_3 \end{bmatrix}, \quad \mathbf{a}(t) = \begin{bmatrix} \mathbf{a}_1(t) \\ \mathbf{a}_2(t) \\ \mathbf{a}_3(t) \end{bmatrix} \quad (2.6)$$

Defining the shape function matrix $\mathbf{S}(\mathbf{x})$, the position vector filed \mathbf{r} could be written through Equation 2.5 as:

$$\mathbf{r}(\mathbf{x}, t) = \mathbf{S}(\mathbf{x})\mathbf{e}(t) \quad (2.7)$$

where $\mathbf{e}(t)$ is the vector of time-dependent parameters and $\mathbf{S}(\mathbf{x}) = \mathbf{P}(\mathbf{x})\mathbf{B}_p^{-1}$ is the space-dependent matrix. Assuming that the continuum body under consideration could be discretized in a number of finite elements equal to n_e , an arbitrary point on the finite element j is defined by the global position vector \mathbf{r}^j as:

$$\mathbf{r}^j(\mathbf{x}^j, t) = \mathbf{S}^j \mathbf{e}^j, \quad j = 1, 2, \dots, n_e \quad (2.8)$$

The shape function matrix $\mathbf{S}^j = \mathbf{S}^j(\mathbf{x}^j)$ depends on the element spatial coordinates $\mathbf{x}^j = [\mathbf{x}_1^j \quad \mathbf{x}_2^j \quad \mathbf{x}_3^j]^T$ that are defined in the element reference configuration. On the other hand, the vector of time-dependent nodal coordinates $\mathbf{e}^j = \mathbf{e}^j(t)$ represents displacements and spatial derivatives at a set of nodal points selected for the finite element.

2.3.3 Unified ANCF Geometry/Analysis Mesh

ANCF finite elements can be used to develop unified and accurate geometry/analysis meshes for the Mars-rover airless tires, thereby avoiding the costly and time consuming conversion of solid models to analysis meshes. In this investigation, fully-parameterized ANCF plate elements are used to create the geometry/analysis mesh of the airless tires. These elements allow for describing an arbitrary stress-free reference-configuration geometry by changing the length and orientation of the nodal position-gradient vectors. A coarse mesh with only four radial elements was found to be sufficient, as shown in Fig. 8. Fully-parameterized ANCF finite elements, which have a complete set of position-gradient vectors, also allow describing geometric discontinuities that may include T- and V-sections. Furthermore, as previously mentioned, ANCF elements allow avoiding geometry distortions that result from converting CAD solid models into FE analysis

meshes (Grossi et al., 2019). The complex airless-tire shape can be obtained by modifying the position-vector gradients at the mesh nodal points at a preprocessing stage. That is, the overall element- and mesh-geometry changes as well as local shape manipulations can be conveniently made using the vector of nodal coordinates in the stress-free reference configuration.

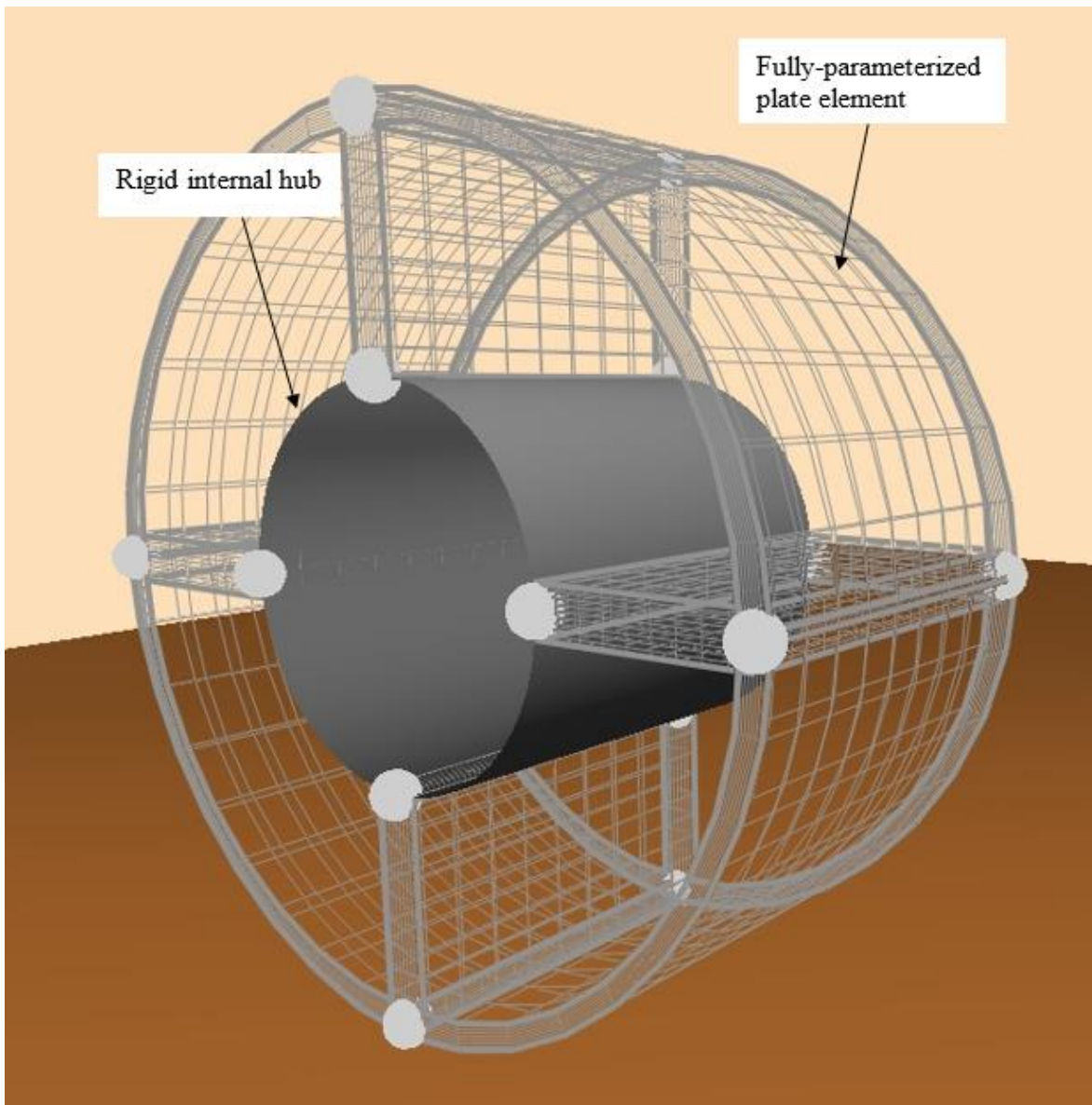


Figure 8. Airless tire mesh developed using ANCF fully parameterized plate elements

In this study, as shown in Fig. 9, the wheel geometry is described using three different sets of coordinates or parameters, namely $\mathbf{x} = [x_1 \ x_2 \ x_3]^T$ associated with the straight configuration,

$\mathbf{X} = [X_1 \ X_2 \ X_3]^T$ associated with the stress-free reference configuration, and $\mathbf{r} = [r_1 \ r_2 \ r_3]^T$ associated with the current deformed configuration. The matrix of position-vector gradients could be described as:

$$\mathbf{J} = \partial \mathbf{r} / \partial \mathbf{X} = (\partial \mathbf{r} / \partial \mathbf{x})(\partial \mathbf{x} / \partial \mathbf{X}) = \mathbf{J}_e \mathbf{J}_o^{-1} \quad (2.9)$$

where $\mathbf{J}_o = \partial \mathbf{X} / \partial \mathbf{x}$ and $\mathbf{J}_e = \partial \mathbf{r} / \partial \mathbf{x}$. The Green-Lagrange strain tensor is defined as:

$$\boldsymbol{\varepsilon} = (1/2) \left[(\mathbf{J}_o^{-1})^T \mathbf{J}_e^T \mathbf{J}_e \mathbf{J}_o^{-1} - \mathbf{I} \right] \quad (2.10)$$

where \mathbf{I} is the 3×3 identity matrix. The straight, current-deformed, and stress-free reference configurations are associated with three different volumes V , v , and V_o , respectively. The relationships between these volumes are $dv = J dV_o$, $dV_o = J_o dv$, and $dv = J_e dV$, where J , J_o , and J_e are the determinants of the gradient matrices \mathbf{J} , \mathbf{J}_o , and \mathbf{J}_e , respectively.

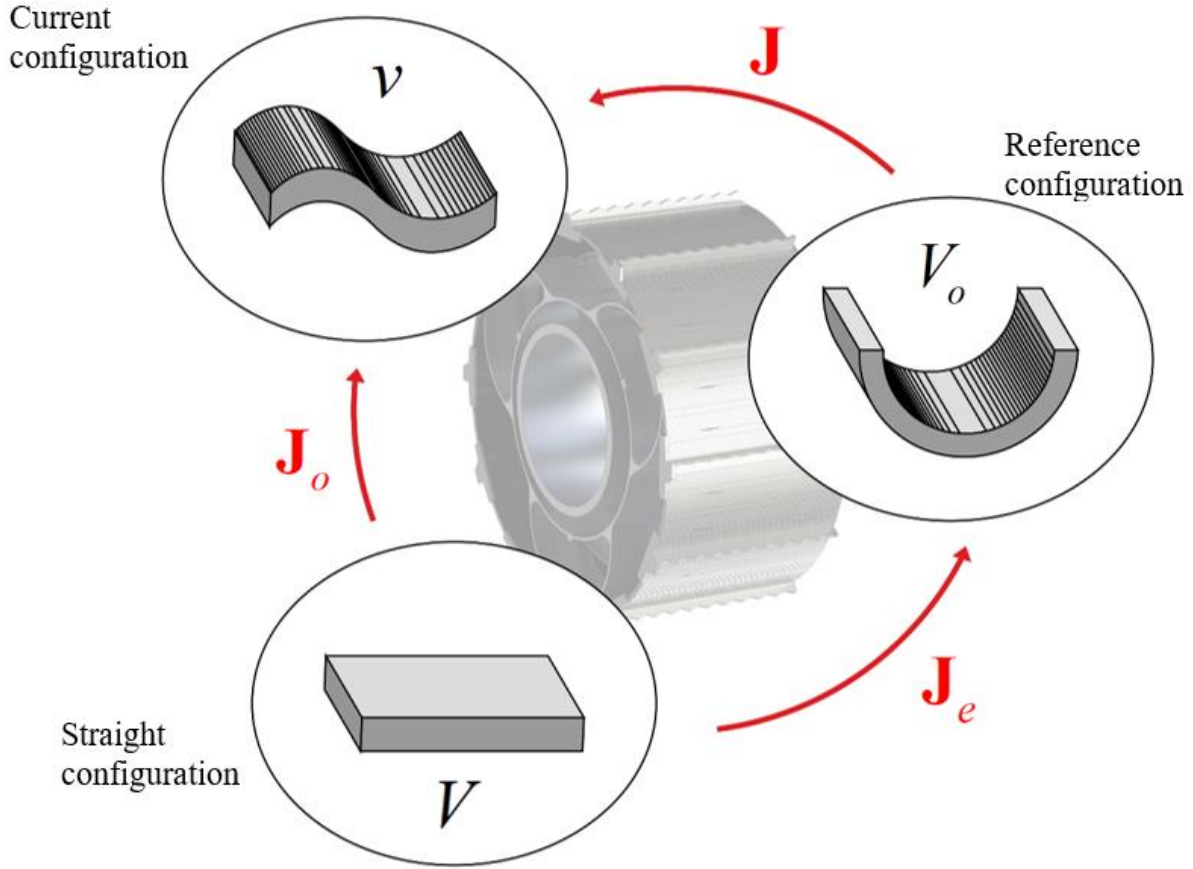


Figure 9. Three geometry configurations

The tires are discretized using fully-parameterized ANCF plate elements. The displacement field of an element j can be written as:

$$\mathbf{r}^j(\mathbf{x}^j, t) = \mathbf{S}^j(\mathbf{x}^j) \mathbf{e}^j(t) \quad (2.11)$$

where \mathbf{S}^j and \mathbf{e}^j are, respectively, the element shape function matrix and the vector of element nodal coordinates. The element shape function matrix is given by:

$$\mathbf{S}^j = \begin{bmatrix} s_1 \mathbf{I} & s_2 \mathbf{I} & s_3 \mathbf{I} & s_4 \mathbf{I} & s_5 \mathbf{I} & s_6 \mathbf{I} & s_7 \mathbf{I} & s_8 \mathbf{I} \\ s_9 \mathbf{I} & s_{10} \mathbf{I} & s_{11} \mathbf{I} & s_{12} \mathbf{I} & s_{13} \mathbf{I} & s_{14} \mathbf{I} & s_{15} \mathbf{I} & s_{16} \mathbf{I} \end{bmatrix} \quad (2.12)$$

where \mathbf{I} is the 3×3 identity matrix and the shape functions s_i , $i = 1, 2, \dots, 16$, are defined as

follows:

$$\left. \begin{aligned}
 s_1 &= -(\xi - 1)(\eta - 1)(2\eta^2 - \eta + 2\xi^2 - \xi - 1), s_2 = -a\xi(\xi - 1)^2(\eta - 1), \\
 s_3 &= -b\eta(\eta - 1)^2(\xi - 1), s_4 = t\zeta(\xi - 1)(\eta - 1), s_5 = \xi(2\eta^2 - \eta - 3\xi + 2\xi^2)(\eta - 1), \\
 s_6 &= -a\xi^2(\xi - 1)(\eta - 1), s_7 = b\xi\eta(\eta - 1)^2, s_8 = -t\xi\zeta(\eta - 1), \\
 s_9 &= -\xi\eta(1 - 3\xi - 3\eta + 2\eta^2 + 2\xi^2), s_{10} = a\xi^2\eta(\xi - 1), s_{11} = b\xi\eta^2(\eta - 1), s_{12} = t\xi\eta\zeta, \\
 s_{13} &= \eta(\xi - 1)(2\xi^2 - \xi - 3\eta + 2\eta^2), s_{14} = a\xi\eta(\xi - 1)^2, \\
 s_{15} &= -b\eta^2(\xi - 1)(\eta - 1), s_{16} = -t\eta\zeta(\xi - 1)
 \end{aligned} \right\} \quad (2.13)$$

and $\xi = x_1^j/a$, $\eta = x_2^j/b$, and $\zeta = x_3^j/t$, and t is the element thickness. The fully parametrized plate element is characterized by four nodes. Twelve coordinates are defined for each node k : three translational ones \mathbf{r}^{jk} , and three vectors $\mathbf{r}_{x_1}^{jk}$, $\mathbf{r}_{x_2}^{jk}$, and $\mathbf{r}_{x_3}^{jk}$ that exemplified the nine gradient coordinates. In the end, each element has a total of 48 nodal coordinates, that could be summarized in a vector form as:

$$\mathbf{e}^j(t) = \left[\mathbf{e}^{j1^T} \quad \mathbf{e}^{j2^T} \quad \mathbf{e}^{j3^T} \quad \mathbf{e}^{j4^T} \right]^T \quad (2.14)$$

where,

$$\begin{aligned}
 \mathbf{e}^{jk} &= \left[\mathbf{r}^{jk^T} \quad (\partial\mathbf{r}^{jk} / \partial x)^T \quad (\partial\mathbf{r}^{jk} / \partial y)^T \quad (\partial\mathbf{r}^{jk} / \partial z)^T \right]^T \\
 &= \left[\mathbf{r}^{jk^T} \quad \mathbf{r}_{x_1}^{jk^T} \quad \mathbf{r}_{x_2}^{jk^T} \quad \mathbf{r}_{x_3}^{jk^T} \right]^T, \quad k = 1, 2, 3, 4
 \end{aligned} \quad (2.15)$$

The vector $\mathbf{e}^j(t)$ can be written in terms of the nodal displacement vector $\mathbf{e}_d^j(t)$ as:

$$\mathbf{e}^j(t) = \mathbf{e}_o^j + \mathbf{e}_d^j(t) \quad (2.16)$$

where \mathbf{e}_o^j is the vector of coordinates in the reference configuration which can be used to define complex stress-free reference configuration plate-mesh geometries.

2.3.4 Structural Discontinuities

The ANCF airless-tire geometry considered in this thesis is characterized by structural discontinuities between radial and circumferential elements, as shown in Fig. 10. At a point or node of discontinuity, the coordinate lines (parameters) are not continuous. Examples of these discontinuities are T- and V-sections, as previously mentioned. At a discontinuity node, two different plate elements have two different sets of gradient coordinates. In order to model the structural discontinuity, the approach adopted by Patel et al. (2019) is used in this investigation.

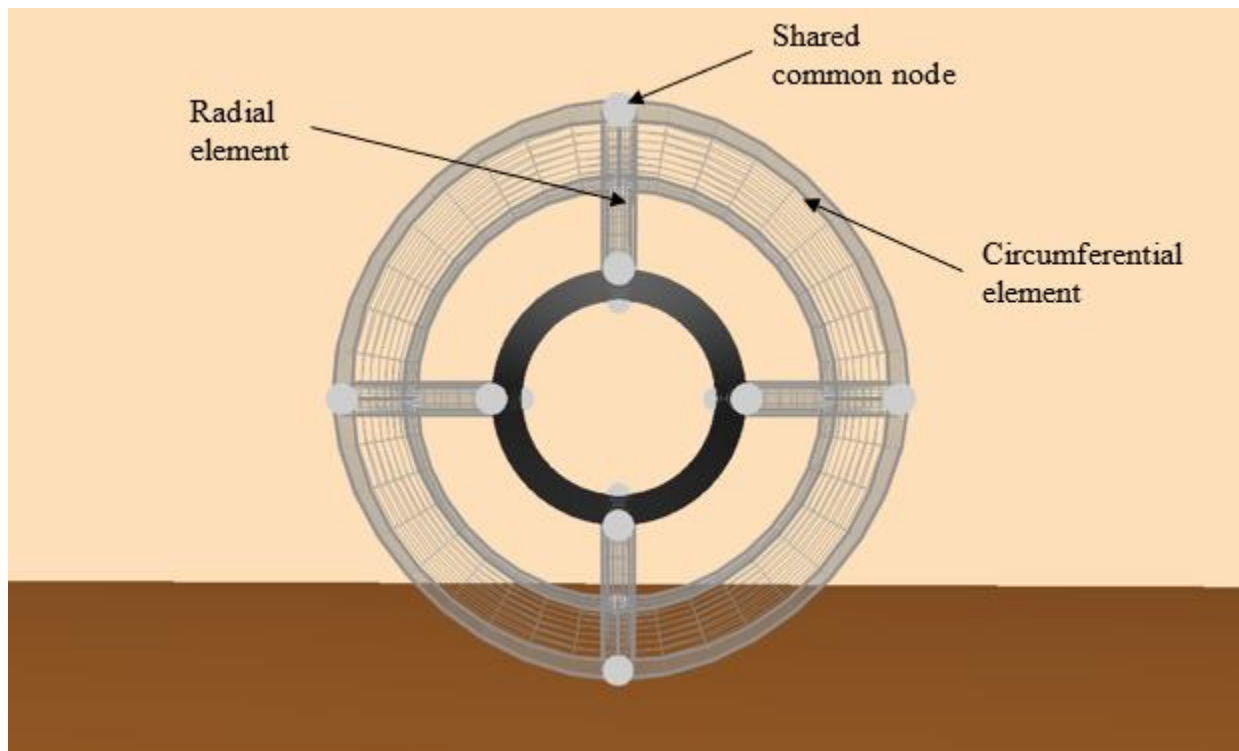


Figure 10. Airless-tire structural discontinuities

The idea is to define the element nodal coordinates in a *structure coordinate system* common to all elements of the FE mesh. In this case, the nodal coordinate vector \mathbf{e}^i of element i can be defined in the structure coordinate system using the gradient transformation \mathbf{T}^i as:

$$\mathbf{e}^i = \mathbf{T}^i \mathbf{p}^i \quad (2.17)$$

where \mathbf{p}^i is the vector of element nodal coordinates defined along the coordinate lines of the structure coordinate system. It is important to emphasize that the transformation matrix \mathbf{T}^i is not in general an orthogonal matrix; it is the matrix obtained by defining the relationship between two different sets of gradient vectors that are tangent to two different sets of coordinate lines (parameters). Using this approach, the connectivity conditions at a discontinuity node k between two elements i and j can be written using the linear algebraic equations:

$$\mathbf{C}^k(\mathbf{p}^i, \mathbf{p}^j) = \mathbf{0} \quad (2.18)$$

where \mathbf{p}^i and \mathbf{p}^j are, respectively, the nodal coordinates of the two elements i and j defined in a common structure coordinate system. The constraint Jacobian matrix between the two elements i and j that share a common node k , can then be defined as:

$$\mathbf{C}_{\mathbf{p}}^k = \begin{bmatrix} \mathbf{C}_{\mathbf{p}^i}^k & \mathbf{C}_{\mathbf{p}^j}^k \end{bmatrix} = \begin{bmatrix} \partial \mathbf{C}^k / \partial \mathbf{p}^i & \partial \mathbf{C}^k / \partial \mathbf{p}^j \end{bmatrix} = \begin{bmatrix} \mathbf{S}^{ki} \mathbf{T}^{ki} & -\mathbf{S}^{kj} \mathbf{T}^{kj} \\ \mathbf{S}_x^{ki} \mathbf{T}^{ki} & -\mathbf{S}_x^{kj} \mathbf{T}^{kj} \\ \mathbf{S}_y^{ki} \mathbf{T}^{ki} & -\mathbf{S}_y^{kj} \mathbf{T}^{kj} \\ \mathbf{S}_z^{ki} \mathbf{T}^{ki} & -\mathbf{S}_z^{kj} \mathbf{T}^{kj} \end{bmatrix} \quad (2.19)$$

where $\mathbf{p} = \begin{bmatrix} \mathbf{p}^{i^T} & \mathbf{p}^{j^T} \end{bmatrix}^T$, \mathbf{T}^{ke} is a partition of the transformation matrix \mathbf{T}^e of element e , $e = i, j$, associated with node k ; $\mathbf{S}_{\alpha}^{ke} = \partial \mathbf{S}^{ke} / \partial \alpha$, $\alpha = x, y, z$, and \mathbf{S}^{ke} is the shape function matrix of element e evaluated at point or node k . Because the Jacobian matrix $\mathbf{C}_{\mathbf{p}^e}^k$ is constant, a constant velocity transformation matrix can be developed for the entire mesh and used to perform a standard FE assembly. This assembly process eliminates the dependent variables at the discontinuity node at a preprocessing stage.

2.3.5 Airless-Tire Assembly

The Mars rover considered in this study has six wheels; each of which can have arbitrarily large displacements including finite rotations. The ability to have this large displacement allows the rover to negotiate, and if necessary, climb very rough terrains that characterize the Mars soil. Because ANCF finite elements can describe arbitrarily large displacements, one *geometry/analysis mesh* can be developed to include the six wheels despite the fact that these wheels can have independent and large displacement with respect to each other. Such a geometry/analysis mesh defines the wheel assembly; and such an assembly, which can be performed at a preprocessing stage, can also include the wheel hubs, axles, and control arms. Using this ANCF assembly procedure, the dependent variables can be eliminated at a preprocessing stage; contributing to reduction in the model dimensionality. This new geometry/analysis mesh can be developed using the concept of the *ANCF reference node* (Shabana, 2014; Shabana, 2015). A salient aspect that should be noted is the fundamental difference between ANCF reference node and the rigid-body element (RBE) used in commercial FE software, as previously discussed in the literature.

As previously mentioned, the ANCF reference node (ANCF-RN), used in the rover hub/wheel assembly, allows defining general connectivity conditions at a preprocessing stage thus eliminating dependent variables resulting from imposing RN constraint equations. While the ANCF-RN is not associated with any particular element of the mesh, it has its own coordinates which consist of one position vector and three position-gradient vectors. In order to connect the ANCF reference node, referred to using the superscript r , with another mesh nodes, referred to using the superscript k , all or a subset of the following linear algebraic constraints can be applied at a preprocessing stage, depending on the number and type of conditions to be imposed:

$$\begin{aligned} \mathbf{r}^k - \mathbf{r}^r &= x^k \mathbf{r}_x^r - y^k \mathbf{r}_y^r - z^k \mathbf{r}_z^r \\ \begin{bmatrix} \mathbf{r}_x^k & \mathbf{r}_y^k & \mathbf{r}_z^k \end{bmatrix} &= \begin{bmatrix} \mathbf{r}_x^r & \mathbf{r}_y^r & \mathbf{r}_z^r \end{bmatrix} \mathbf{J}^{kr}, \quad k = 1, \dots, m_r \end{aligned} \quad (2.20)$$

where \mathbf{r} is the global position vector of the node; x^k , y^k , and z^k represent the Cartesian coordinates of the tire interface node k in the reference configuration (express with respect to the reference node r); \mathbf{J}^{kr} is a constant matrix of position gradients defined in the reference configuration by the equation $\mathbf{J}^k = \mathbf{J}^r \mathbf{J}^{kr}$ in which the matrix \mathbf{J}^i contains the position vector gradients associated with the node $i = k, r$; and m_r is the total number of nodes that have constraints with the reference node. The reference node used in this investigation for the wheel assembly is shown in Fig. 11. A reference node can be used to represent a rigid hub or axle as discussed in the literature.

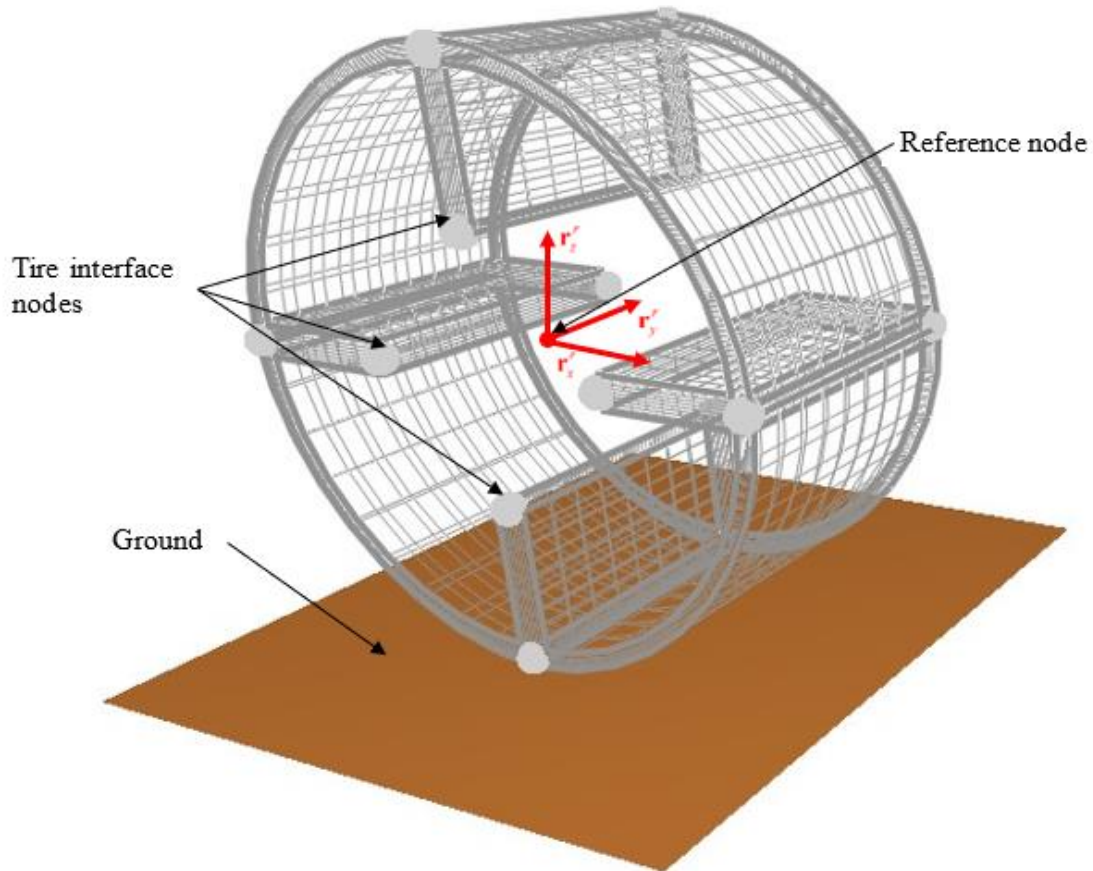


Figure 11. ANCF reference node

2.4 Traction and Tire Contact Forces

The wheel/soil interaction represents one of the main concerns when performing the MBS computer simulations of the rover system. In this section, the tire contact and traction force model used in this investigation are discussed.

2.4.1 Tire Contact Algorithm

In order to evaluate the tire/terrain interaction forces, a point grid is defined on the outer surface of the tire. The same grid is used to search for the contact points using a point-search algorithm that could be summarized through the following procedure:

1. A check is made to determine the distance of the tire finite elements from the ground in order to focus the contact search on a smaller number of elements.
2. On the elements, which can come in contact with the ground, a point grid on the outer surface of the element is defined. This grid defines a sufficient number of points necessary for an accurate distribution of the contact forces.
3. The global position and gradient vectors of the grid points are determined and used to check whether or not these points are in contact with the ground. The position gradients in the element tangent plane are used to determine the normal to the surface at the grid point.
4. If a point on the finite element is in contact with the ground, the normal contact force is computed with a penalty force model which contain stiffness and damping coefficients provided by the user.
5. The relative velocities between the element grid points and the ground are computed. If the tangential relative velocity at a point is different from zero, a tangential friction force with a friction coefficient provided by the user is introduced.
6. The normal and tangential contact forces define the contact-force vector which is used to

determine the generalized contact forces associated with the plate element nodal coordinates. Since multiple contact points may exist, the ANCF generalized forces must account for the forces at all the contact points on the finite elements.

Following a procedure similar to the one used by Patel et al. (2016), the penalty contact force vector is defined as:

$$\mathbf{f}_c = \mathbf{f}_n + \mathbf{f}_t \quad (2.21)$$

where \mathbf{f}_t is the tangential friction force and \mathbf{f}_n is the normal contact force. In this investigation, the normal contact force is defined as:

$$\mathbf{f}_n = (k_n \delta + c_n \dot{\delta}) \mathbf{n} \quad (2.22)$$

where k_n and c_n are, respectively, penalty stiffness and damping coefficients, δ is the penetration, and $\mathbf{n} = (\mathbf{r}_{x_1} \times \mathbf{r}_{x_2}) / |\mathbf{r}_{x_1} \times \mathbf{r}_{x_2}|$ is the unit normal to the surface referred to the position of the contact point. If the relative velocity at the contact point is different from zero, the tangential friction force is defined as $\mathbf{f}_t = -\mu_t |\mathbf{f}_n| \mathbf{t}$, where μ_t is the friction coefficient and \mathbf{t} is a unit vector in the direction of the relative velocity vector at the contact point. The normal and tangential contact forces at the contact points are used to define the generalized contact forces associated with the tire mesh nodal coordinates. An illustration of the contact force model used in this study is shown in Fig. 12.

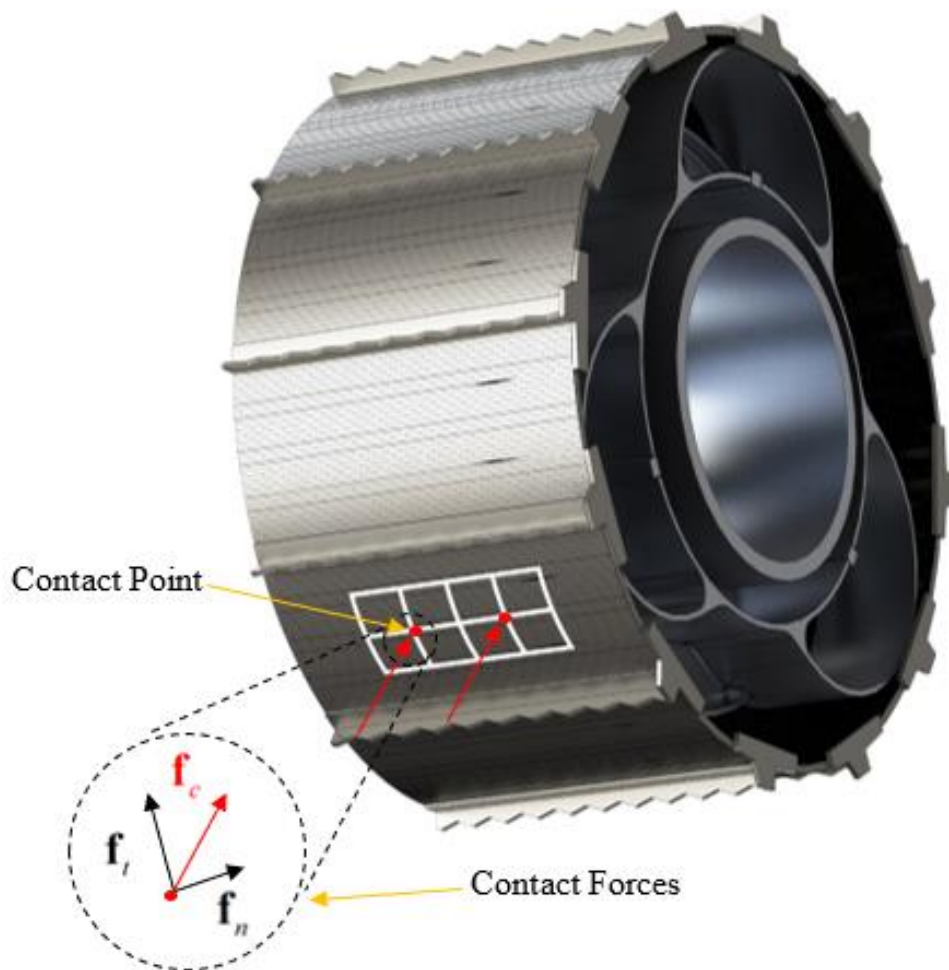


Figure 12. Contact forces

2.4.3 Tractive Forces

In general, the tractive forces, which influence the energy consumptions of planetary rovers, depend on the tangential friction forces as well as other forces such as the wind resistance. In this thesis, the focus will be mainly on the tire tangential friction forces in order to compare between the discrete brush and continuum-based ANCF tire models. The tractive forces resulting from the wheel/soil contact allow the rover to negotiate rough terrains by moving forward, climbing slopes, and passing over obstacles. Wheel slippage and lack of traction can lead to more energy

consumption and to deterioration of the performance in the planetary rovers designed to perform sophisticated tasks by following specified motion trajectories. To enhance the low traction of the soft and sandy Mars soil, grousers are often installed on the external surface of the tire. Increased traction can also be achieved by maximizing the wheel/soil contact area. A larger contact patch can be obtained by increasing the wheel diameter (Siddiqi et al., 2006; Schmid et al., 1995) and/or by using flexible wheels. Due to the mass and dimension constraints that characterize Mars rovers, increasing the wheel dimensions may not be a feasible option. An alternative is to use flexible metal wheels or pneumatic tires. In general, pneumatic tires (Meirion-Griffith et al., 2011; Irani et al., 2011; Ding et al., 2011) are avoided in the design of planetary rovers due to risk of tire puncture, which could compromise the space mission success. Furthermore, pneumatic tires can become brittle at the low Mars-temperatures. Use of flexible metal wheels presents the only effective option that allows for having a large contact patch, reducing slipping, and avoiding sinkage (Ding et al., 2014; Petersen et al., 2011). Several models were developed in the literature to characterize the wheel/soil contact. Bauer et al. (2005) and Scharringhausen et al. (2009) developed rigid wheels for rover applications. Peterson et al. (2011) studied a volumetric contact modelling approach for determining closed-form expressions for the rover tire contact forces. A rigid wheel model that considers slip sinkage was developed by Ding et al. (2014). Flexible wheels were also discussed by different authors (Ishigami et al., 2011; Petersen et al., 2011). Favaedi et al. (2011) predicted the tractive performance of planetary rovers, considering a geometry model of the wheel under deformation. Wanga et al. (2019) presented a model for the interaction between a flexible metal wheel and deformable terrain and analyzed sinkage and drawbar pull in rover applications.

In this thesis, the rover tractive forces are examined using both brush and ANCF airless tires. The brush tire/soil contact is described in detail in the literature (Gipser, 2005; Lugner et al., 2005;

Pacejka, 2006). The contact between the ANCF wheel and the rigid ground is determined as previously discussed in this section using a penalty approach. The normal force is used to determine the tangential friction force that enters into the formulation of the tractive forces. For ANCF airless tires, a point mesh is created on each element and this mesh is used to determine the tire/terrain contact points using a search algorithm. The relative velocities at the contact points are determined, and if this relative velocity is different from zero the friction force at this contact point is computed and applied. It is, however, important to point out that in the steady-state motion, the relative displacement between the tire and the ground is predominantly rolling. In the case of a flexible tire, the oscillations of the material points can lead to change in the direction of the relative velocity because in the case of predominant rolling, the slip is small. In a later section of this thesis, the tangential friction forces predicted using the brush and ANCF tires are compared in an acceleration scenario along a straight path.

2.5 Geometry/Analysis Integration

Successful geometry/analysis integration is necessary for having a science-based computer-aided engineering (CAE) process for the virtual prototyping and design of space vehicles. As discussed in Section 2.3, use of ANCF finite elements allows developing a unified geometry/analysis mesh and avoiding the costly, time-consuming, and error-prone process of converting CAD solid models to FE analysis meshes. In this investigation, one computational environment is used for the geometry and analysis steps, and therefore, the CAD/FE mesh conversion is avoided. In this computational environment, the geometry/analysis mesh is first developed and new concepts, such as the ANCF reference nodes, are used in the model assembly. The geometric, material, and reference configuration data of the assembled mesh are defined and used as input to the MBS algorithm that constructs and numerical solves the rover DAEs system.

The use of this new geometry/analysis approach allows for eliminating a large number of dependent coordinates before the start of the nonlinear dynamic simulations.

2.5.1 Reference-Configuration Geometry and Elastic Forces

The use of the position gradients for developing the solid model of the airless tires, which are assembled at a preprocessing stage using the ANCF reference nodes, allows describing arbitrary geometry and accounting for discontinuities. The same geometry mesh is considered as the analysis mesh and used to define the tire elastic forces due to their deformation resulting from the tire/terrain interaction and other rover forces. Because of the use of the fully-parameterized plate element, the method of general continuum mechanics can be applied for defining the tire elastic forces. The virtual work of the tire elastic forces can be defined for an arbitrary element in the geometry/analysis mesh as:

$$\delta W_s = - \int_{V_o} \boldsymbol{\sigma}_{P2} : \delta \boldsymbol{\varepsilon} dV_o = - \mathbf{Q}_s^T \delta \mathbf{e} \quad (2.23)$$

where V_o is the element volume in the reference configuration, $\boldsymbol{\varepsilon}$ is the Green-Lagrange strain tensor, $\boldsymbol{\sigma}_{P2}$ is the second Piola-Kirchhoff stress tensor, and \mathbf{Q}_s is the vector of generalized elastic forces (Shabana, 2018). As previously discussed, the stress-free reference-configuration of the tire is accounted for using the form of Green-Lagrange strain tensor $\boldsymbol{\varepsilon}$, where the matrices that appear in this equation are as previously defined in this thesis. The vector of elastic force \mathbf{Q}_s is introduced to the equations of motion in the generalized force vector associated with the ANCF nodal coordinates.

2.5.2 Constrained Dynamic Equations

Nonlinear constraint equations which cannot be eliminated at the preprocessing stage are formulated using a set of algebraic equations that can be defined in a vector form as:

$$\mathbf{C}(\mathbf{q}_r, \mathbf{p}, t) = \mathbf{0} \quad (2.24)$$

where \mathbf{q}_r is the vector of coordinates of the rigid bodies in the rover system, \mathbf{p} is the vector of coordinates of the ANCF bodies, and t is time. The vector of nonlinear constraint equations (2.24) that describes specified motion trajectories and mechanical joints can be combined with the second-order differential equations of motion using the vector of Lagrange multipliers $\boldsymbol{\lambda}$. To this end the vector of constraint equations (2.24) is differentiated twice with respect to time to obtain $d^2\mathbf{C}/dt^2 = \mathbf{0}$. This equation leads to

$$\mathbf{C}_{q_r} \ddot{\mathbf{q}}_r + \mathbf{C}_p \ddot{\mathbf{p}} = \mathbf{Q}_c \quad (2.25)$$

In this equation, \mathbf{Q}_c is the vector that absorbs terms which are not linear in the accelerations and result from differentiating the constraint equations twice with respect to time. Using the preceding equation, one can write the augmented form of the equations of motion as (Shabana, 2020)

$$\begin{bmatrix} \mathbf{M}_r & \mathbf{0} & \mathbf{C}_{q_r}^T \\ \mathbf{0} & \mathbf{M}_p & \mathbf{C}_p^T \\ \mathbf{C}_{q_r} & \mathbf{C}_p & \mathbf{0} \end{bmatrix} \begin{bmatrix} \ddot{\mathbf{q}}_r \\ \ddot{\mathbf{p}} \\ \boldsymbol{\lambda} \end{bmatrix} = \begin{bmatrix} \mathbf{Q}_r \\ \mathbf{Q}_p \\ \mathbf{Q}_c \end{bmatrix} \quad (2.26)$$

In this equation, \mathbf{M}_r and \mathbf{M}_p are the mass matrices associated with the rigid-body and ANCF coordinates, respectively; and \mathbf{Q}_r and \mathbf{Q}_p are the force vectors associated, respectively, with the rigid-body and ANCF coordinates. The tire/terrain contact forces are introduced to the dynamic formulation as generalized forces in the vector \mathbf{Q}_p .

2.5.3 Computational Considerations

In the preceding equation, the mass matrix \mathbf{M}_p and the force vector \mathbf{Q}_p are the mass matrix and force vector of the geometry/analysis mesh obtained for the rover tire assembly. Therefore, in this investigation, all the rover tires are treated as one subsystem that has one inertia matrix and one force vector. In the numerical implementation, the ANCF Cholesky coordinates are used in order to obtain an identity generalized mass matrix, that is, $\mathbf{M}_p = \mathbf{I}$ and the vector \mathbf{p} is the vector of ANCF Cholesky coordinates (Shabana, 2018). This ensures that the coefficient matrix in the augmented Lagrangian equation is a sparse matrix; allowing for using sparse matrix techniques to obtain an efficient solution. The preceding augmented Lagrangian equation is solved for the vectors of accelerations $\ddot{\mathbf{q}}_r$ and $\ddot{\mathbf{p}}$ as well as the vector of Lagrange multipliers $\boldsymbol{\lambda}$. In order to compute the coordinates and velocities, the independent accelerations are identified and integrated forward in time. The MBS numerical algorithm used in this study to solve the Mars rover equations is designed to ensure that all the nonlinear constraint equations $\mathbf{C}(\mathbf{q}_r, \mathbf{p}, t) = \mathbf{0}$ are satisfied at the position, velocity, and acceleration levels.

CHAPTER 3

NUMERICAL RESULTS

In this chapter, several tests are performed in order to evaluate the accuracy and efficiency of the geometry/analysis approach used in this study to solve the rover nonlinear dynamic equations. Two different rover models are considered in this numerical study. In the first model, the rover tires are modeled using the discrete brush-type approach, while in the second model, continuum-based ANCF tires are used. The simulations are performed using the general-purpose MBS software **Sigma/Sams** (Systematic Integration of Geometric Modeling and Analysis for the Simulation of Articulated Mechanical Systems). Because it was not possible for the authors to obtain the exact measurements and material properties of the components of the Mars rover considered in this study, all the numerical results presented in this chapter should be interpreted as a qualitative assessment of the rover dynamic behavior and as qualitative comparison between the two tire models considered in this investigation.

3.1 Rover Model Description

Figure 13 shows the components of the wheeled robot used in this numerical investigation. The inertia properties of different components are provided in Table 1, where I_{xx} , I_{yy} , and I_{zz} are the mass moments of inertia.

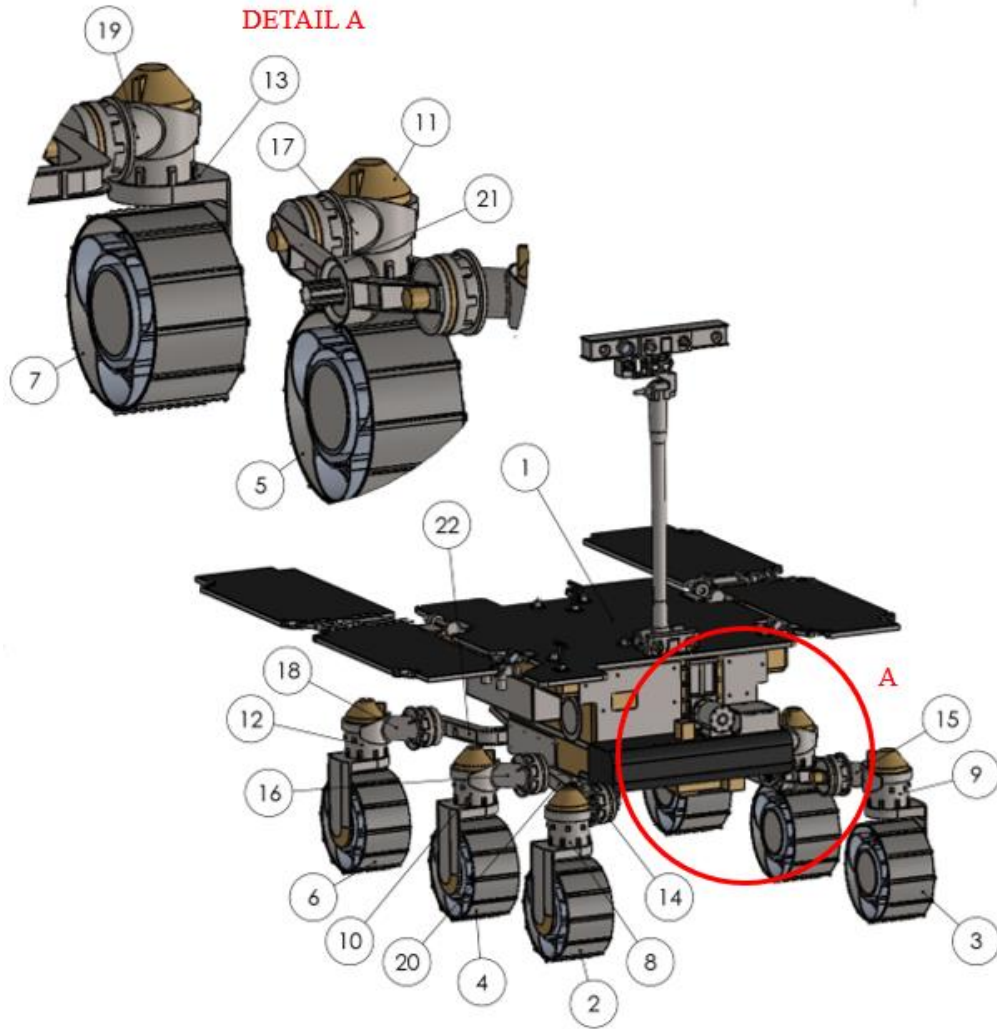


Figure 13. Components of the rover

TABLE I. ROVER INERTIA PROPERTIES

Body Number	Component	Mass (kg)	I_{xx} (kg.m ²)	I_{yy} (kg.m ²)	I_{zz} (kg.m ²)
1	Principal	246.39796	51	65	98
2, 3, 4, 5, 6, 7	Wheel	4.44157	0.05941	0.08571	0.05941
8, 9, 10, 11, 12, 13	Spindle	4.27728	0.14314	0.12524	0.04277
14, 15, 16, 17, 18, 19	Arm	1.74699	0.01933	0.00691	0.01769
20, 21	Pivot lateral	2.53122	0.00459	0.09341	0.09112
22	Pivot rear	5.74456	0.97106	1.07547	0.11176
23	Ground	0	0	0	0

The mass of the vehicle is approximately 320 kg. The actuators are defined using 21 revolute joints. Figure 14 shows the connections of different components in one of the bogie structures of the vehicle.

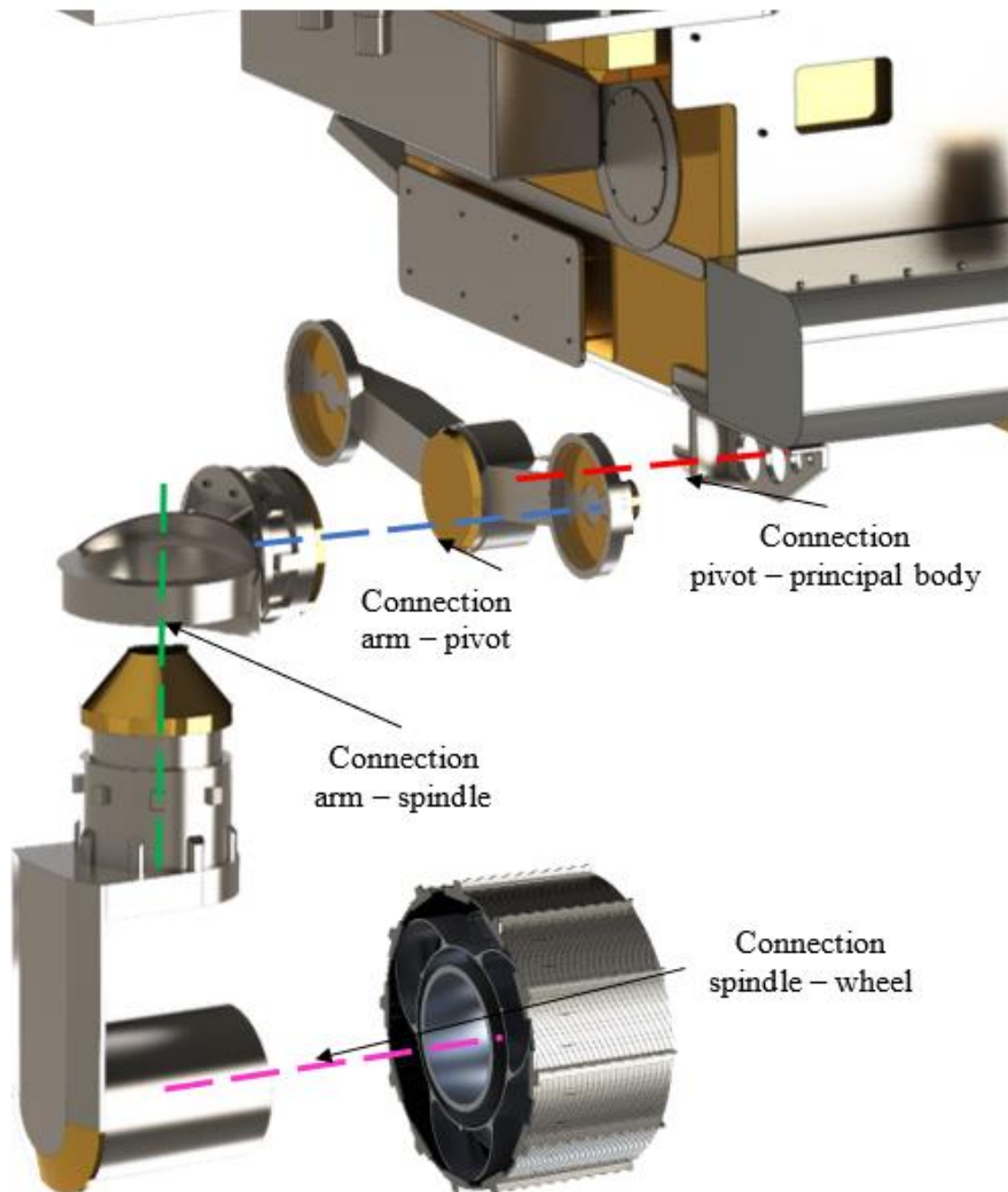


Figure 14. Rover revolute joints

The weight distribution among different wheels is calculated using static equilibrium analysis, as shown in Fig. 15.

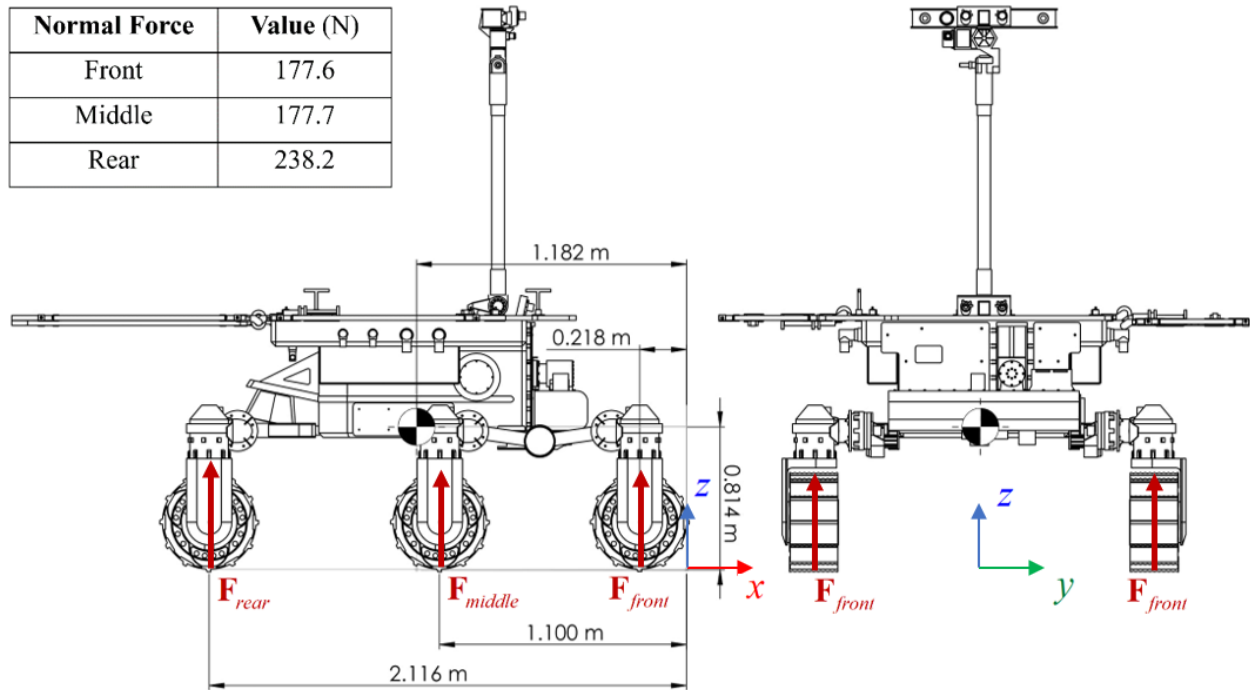


Figure 15. Weight distribution on the rover wheels

3.2 Brush-Type Rover Model

In this first numerical example, the wheels are defined using a discrete brush-type model which does not account for the distributed inertia and elasticity. The initial system configuration is depicted in Fig. 16.

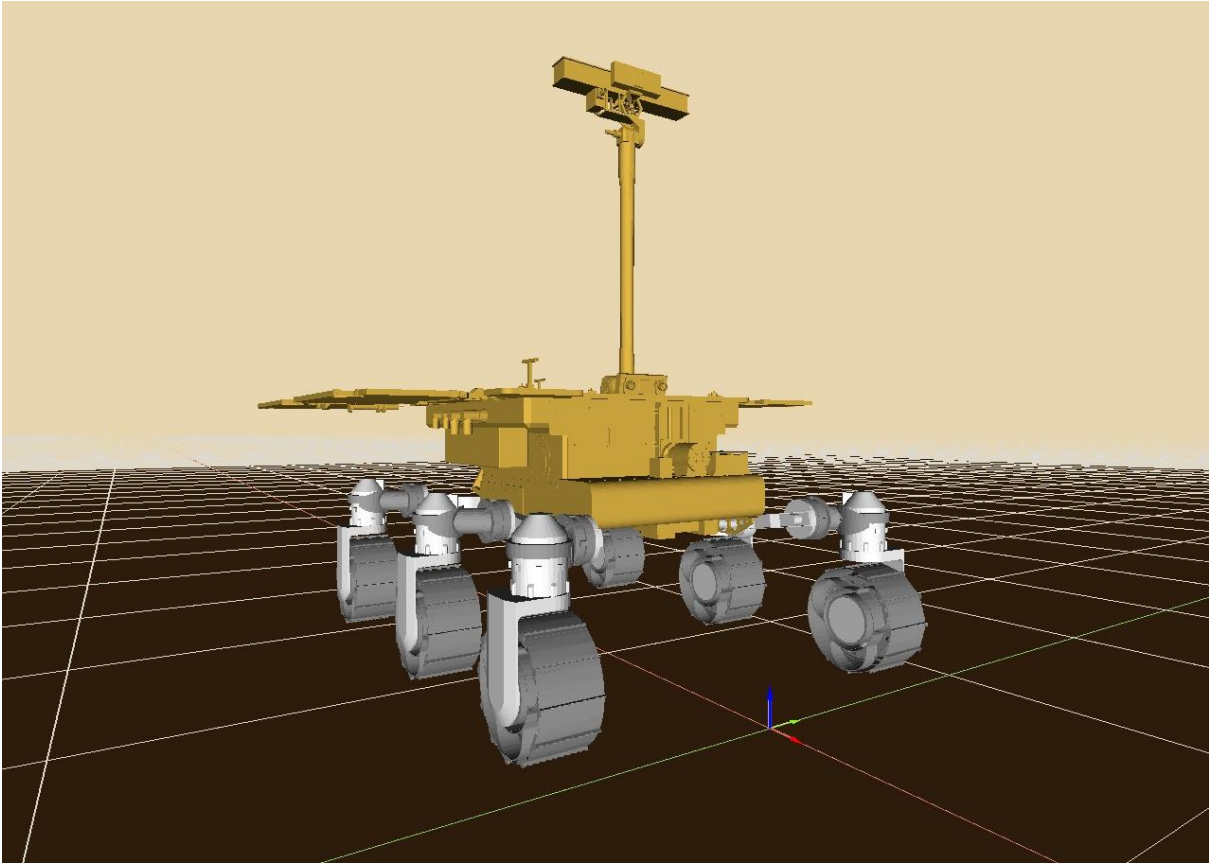


Figure 16. Rover model with the brush-type tires

For the purpose of verifying the results obtained in this numerical investigation, the average stiffness curve obtained by Sivo et al. (2019) and shown in Fig. 17 is considered.

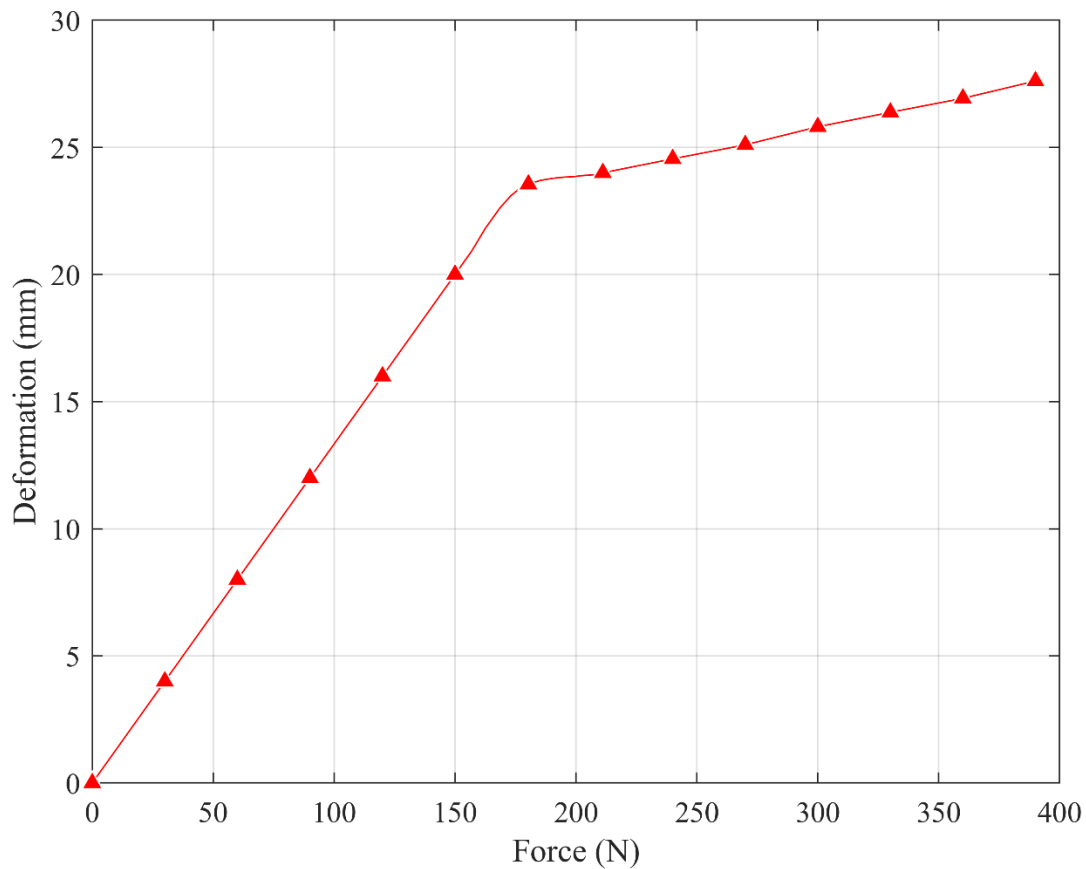


Figure 17. Average stiffness curve (Sivo at al., 2019)

As previously mentioned, because of the rover wheel configuration, the radial stiffness of the wheel varies along the circumferential direction. If a brush-type tire model is used, this radial stiffness variation cannot be easily captured because of the simplicity of the approach. For this reason, the results can only be verified against an average stiffness curve. In the first dynamic simulation scenario performed, a free fall of the rover on the ground, starting from a height of 10 mm, is considered. For each wheel, the force acting on the wheel center of mass and the wheel deformation are measured. The wheel normal contact forces and radial deformations are shown in Figs. 18 and 19, respectively.

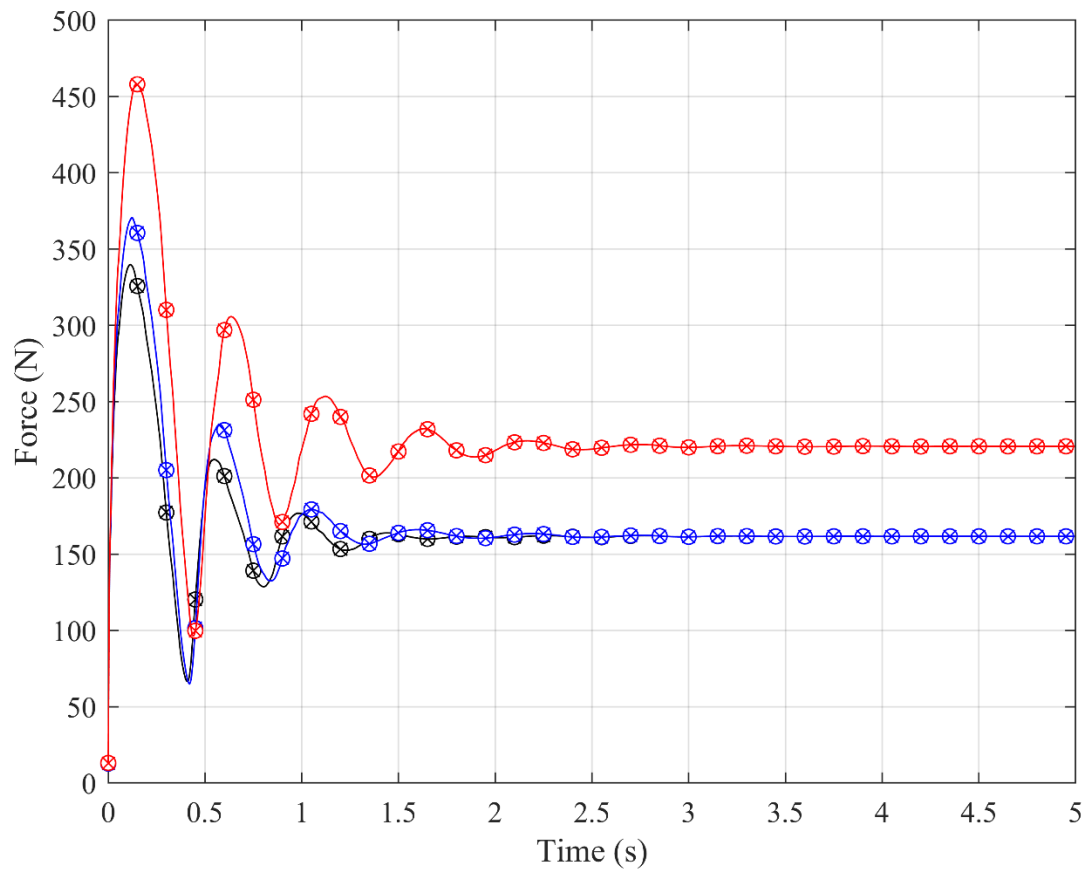


Figure 18. Vertical force on a brush-type tire in the free fall scenario

(—○— Front Right, —×— Front Left, —○— Middle Right, —×— Middle Left,
 —○— Rear Right, —×— Rear Left)

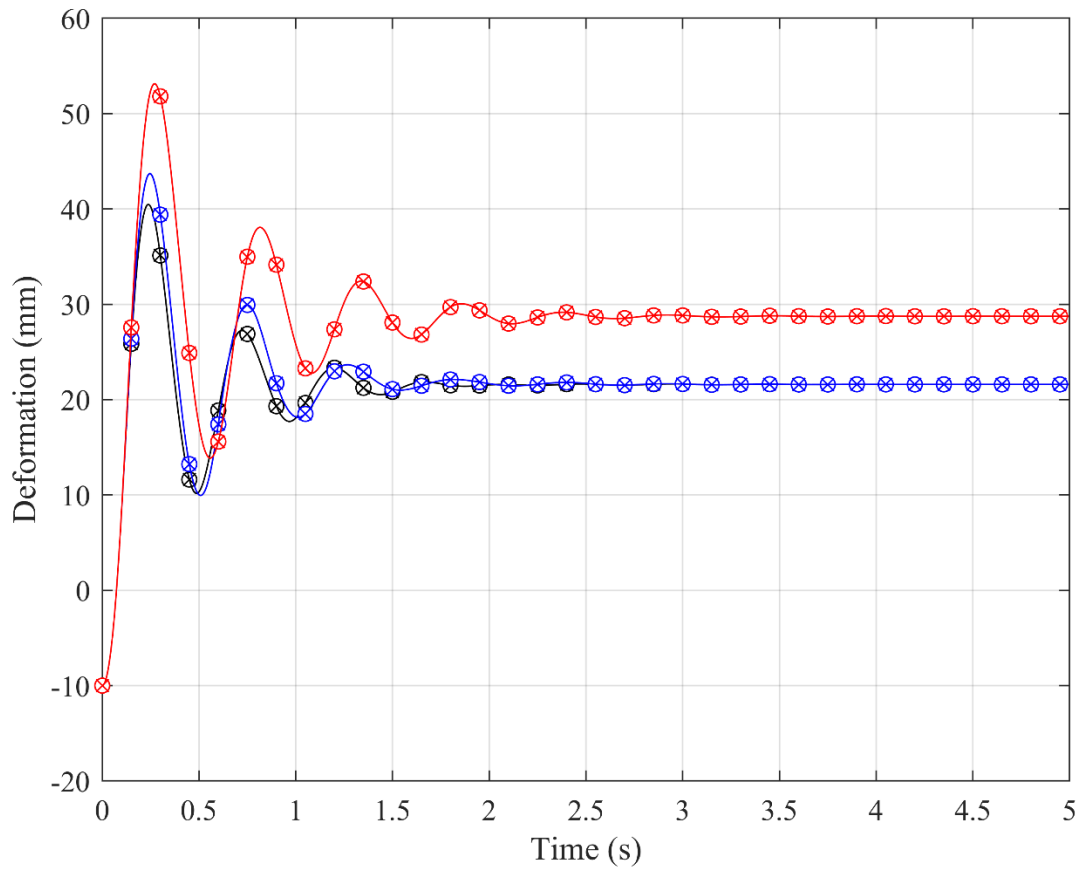


Figure 19. Deformation of a brush-type tire in the free fall scenario

(—○— Front Right, —×— Front Left, —○— Middle Right, —×— Middle Left,
 —○— Rear Right, —×— Rear Left)

The results shown in Fig. 18 are in agreement with the results obtained using a static analysis. The brush tire parameters used in this problem are defined using a tuning procedure and are reported in Table 2.

TABLE II. BRUSH-TYPE TIRE PARAMETERS

Parameter	Value
Radial stiffness (N/m)	8250
Radial damping (N·s/m)	8140
Longitudinal slip stiffness (N/m ²)	8250
Lateral slip stiffness (N/deg·m ²)	850
Minimum friction coefficient	0.597
Maximum friction coefficient	0.757
Rolling resistance coefficient	0.015

The vertical force acting on the principal body of the rover was gradually increased, so that each wheel would be subjected to a normal load in the range of 160–250 N. The results obtained are compared with the reference numerical results of Sivo et al. (2019), as shown in Fig. 20.

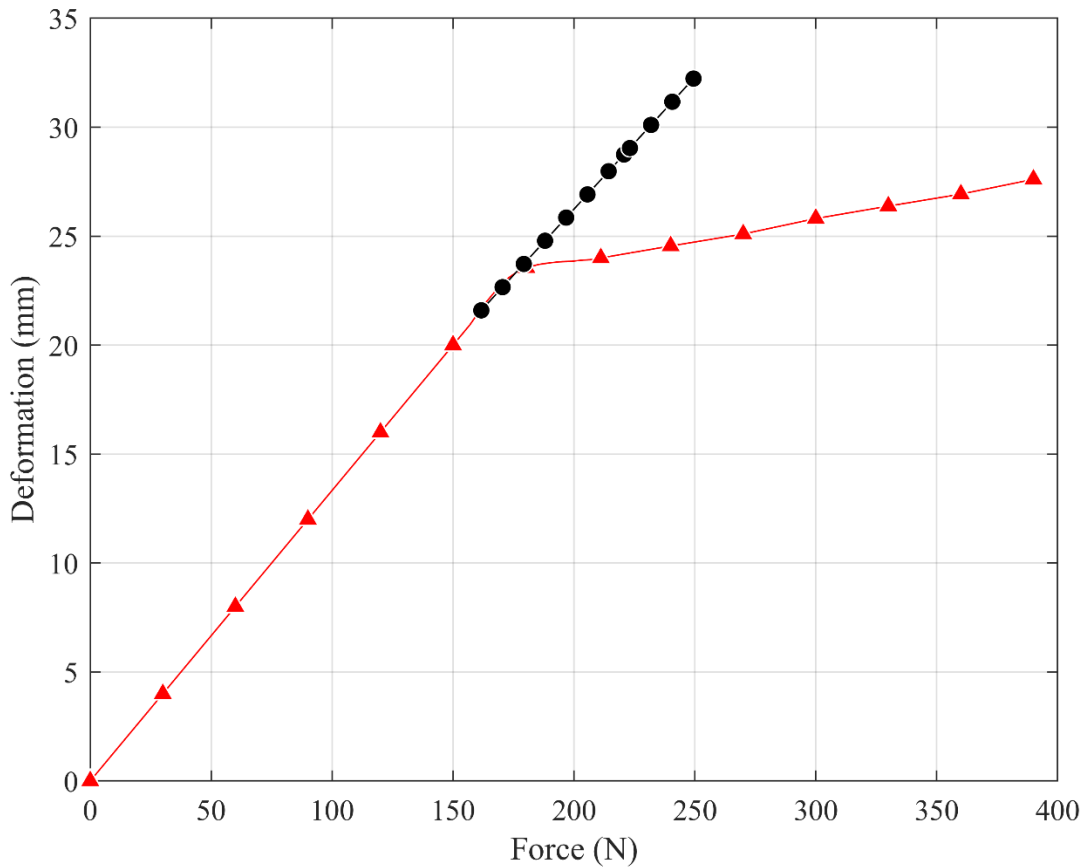


Figure 20. Verification of the brush-type tire model

(—▲— Average Curve, —●— Brush-type Tire)

It is observed that the brush-type tire results match the reference results only when small deformations are considered. As the load increases, the brush-type wheel model fails to capture the material and geometric nonlinearities. Because the rover wheels experience, in general, large deformations, it is clear that the discrete brush-type approach cannot be used to produce accurate results.

3.3 ANCF Airless Tires

Using the ANCF approach, each tire is modeled as a simple cylinder with four radial elements. The wheel mesh consists of eight fully-parameterized plate elements and one ANCF reference

node rigidly connected to the eight internal nodes of the rigid inner hub. The material properties are defined as density $\rho = 1500 \text{ kg/m}^3$, Young modulus $E = 280000 \text{ Pa}$, and Poisson ratio $\nu = 0$. Material damping is introduced using the approach proposed by Grossi and Shabana (2019). The stiffness, damping, and friction coefficients used in the contact force model are defined as $k = 1000 \text{ N/m}$, $c = 100 \text{ Ns/m}$ and $\mu = 0.6$, respectively. The initial configuration of the rover with the ANCF wheels is shown in Fig. 21.

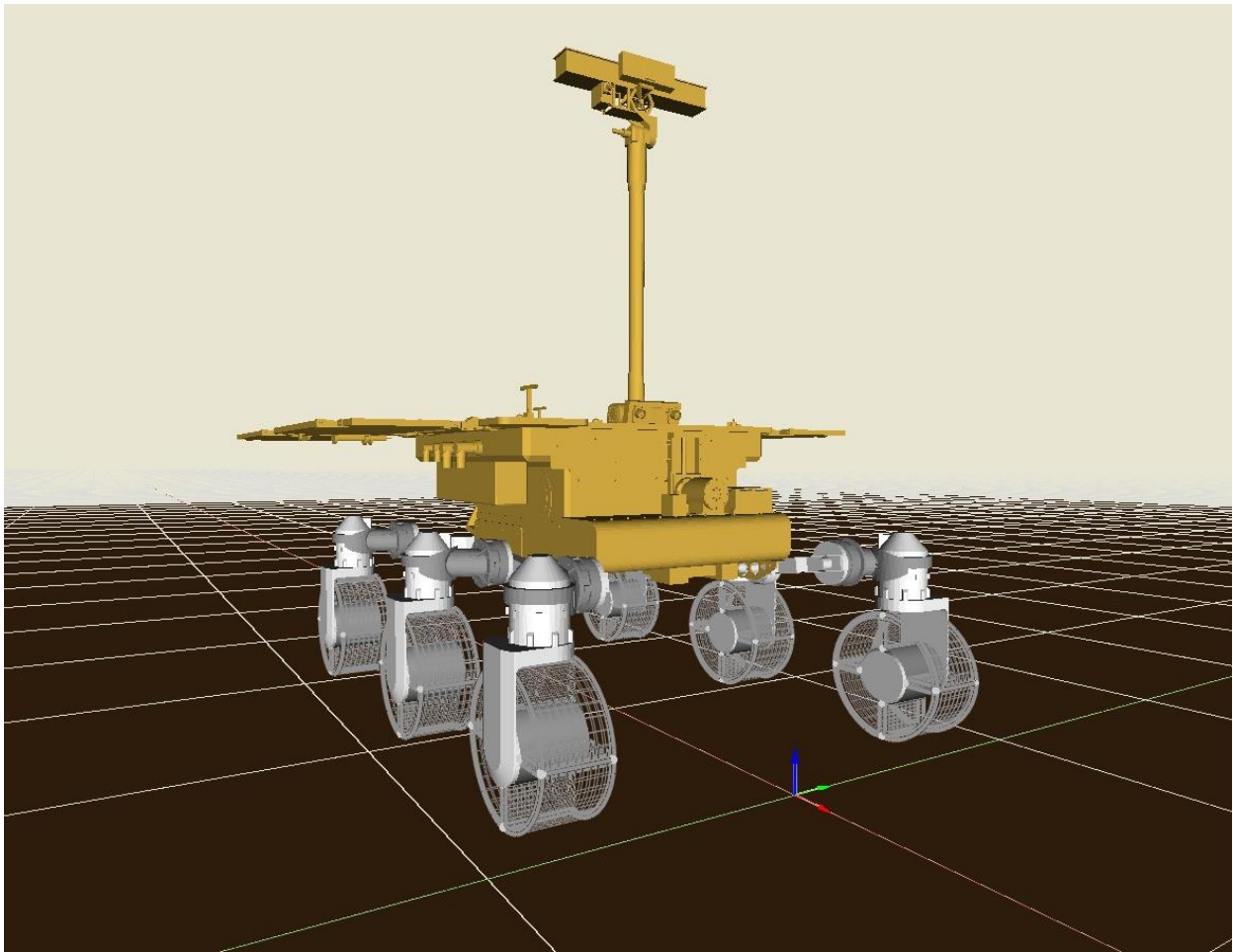


Figure 21. Rover model with ANCF airless tires

The reference results for this analysis are shown in Fig. 7. Following a similar procedure to what described in the previous section, two different force-deformation curves are found. These two

different curves, shown in Fig. 22, are associated with different circumferential orientations of the wheel. It is clear that the two curves are in good agreement with the reference results.

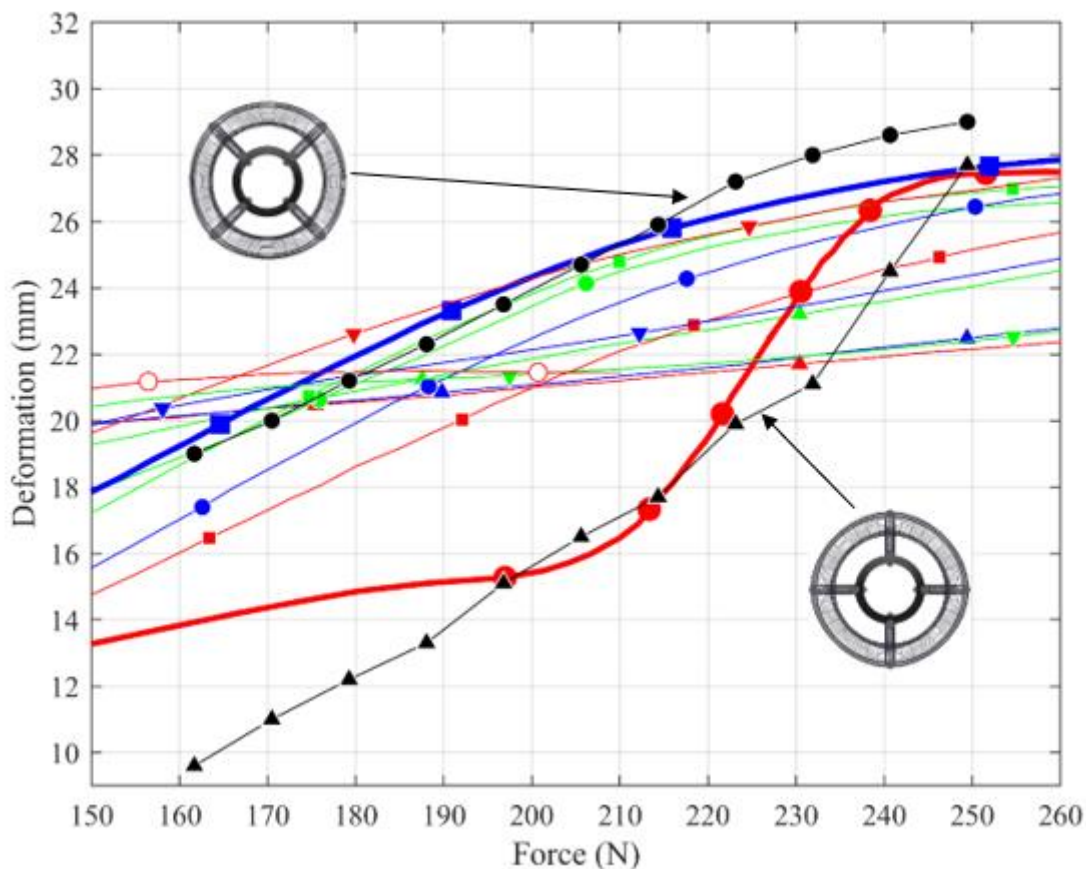


Figure 22. Verification of the ANCF airless tire

(Wheel circumferential orientation: \blacktriangle 0°, \blacktriangle 5°, \blacktriangle 10°, \bullet 15°,
 \bullet 25°, \bullet 30°, \blacksquare 35°, \blacksquare 40°, \blacksquare 100°, \blacktriangledown 105°,
 \blacktriangledown 110°, \blacktriangledown 115°, \circ 120°, \bullet ANCF 45°, \blacktriangle ANCF 0°)

3.4 Comparative Study

The two MBS rover models considered in this section have identical data except for the wheel

modeling approach used. In the first rover model, the discrete brush-type model is used, while in the second approach the continuum-based ANCF model is used. In order to compare between the two models in a dynamic motion scenario, the rover is assumed to negotiate a straight path by reaching its average locomotion speed of 70 m/h. The vehicle is dropped on the ground and allowed to reach its static equilibrium configuration. Subsequently, angular velocity constraints are applied to each wheel, to initiate the forward motion of the vehicle. The vehicle accelerates for 5 s until the desired velocity is reached. The overall computer simulation of 40 s includes also a deceleration of the rover during the last 5 s. The forward velocity of the principal body during the simulation is shown in Fig. 23.

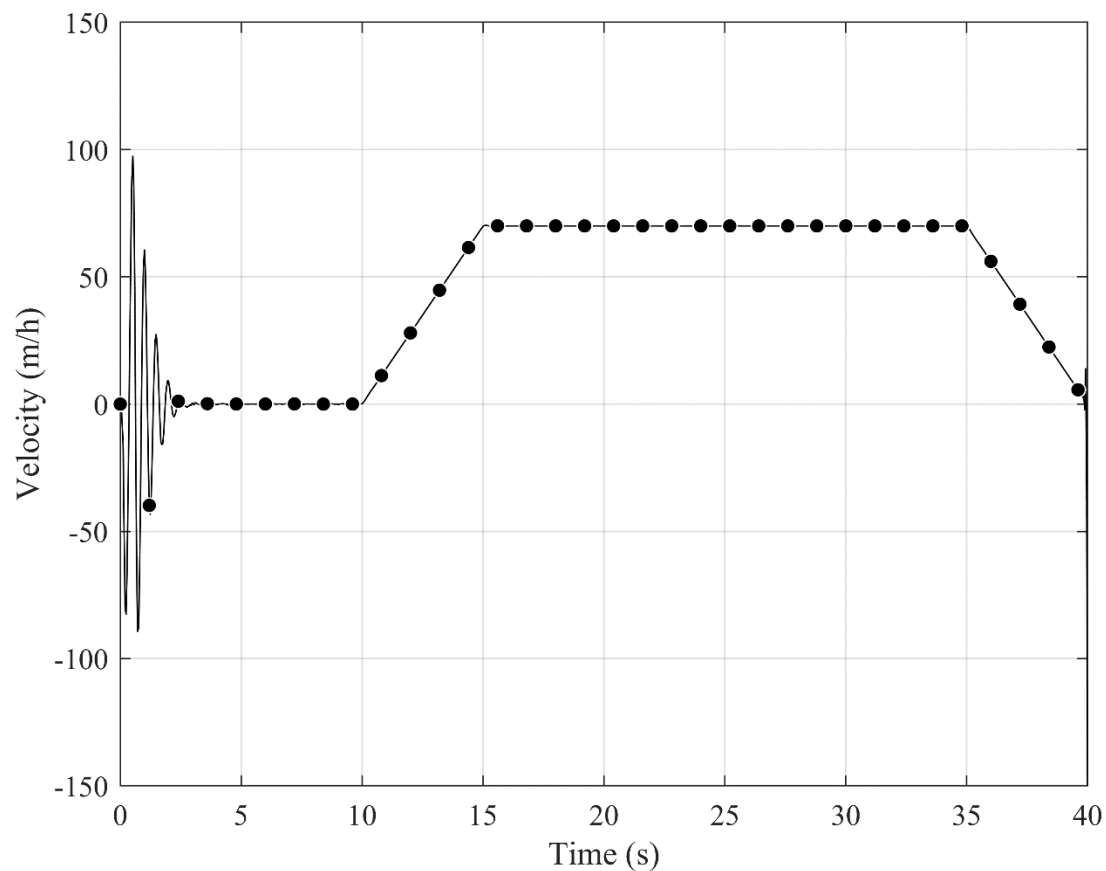


Figure 23. Forward velocity of the principal body

Figure 24 shows the deformation of the right wheel for the two tire models, in the interval of time between 15 and 35 seconds. It is observed that the brush-type wheel behaves identically for all the circumferential positions, thus resulting in a constant deformation. On the other hand, the ANCF-wheel deformation changes as function of the circumferential orientation. This behavior is expected because the radial stiffness of the ANCF wheel varies depending on the wheel orientation.

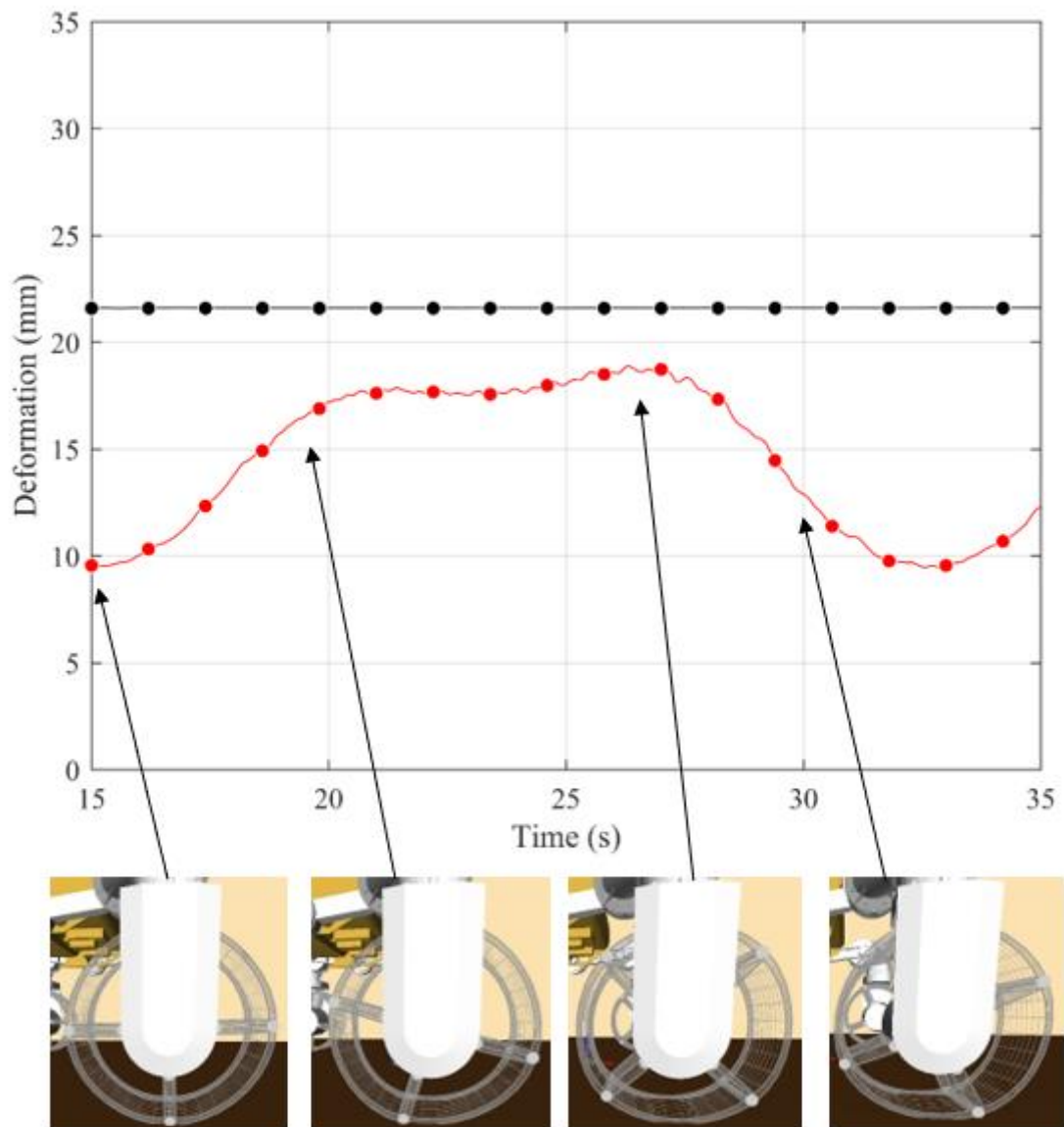


Figure 24. Comparison between brush-type and ANCF airless tires

(—●— Right Front ANCF airless tire, —●— Right Front Brush-type Tire)

While there is still room for further improvements and algorithm optimization to enhance the computational efficiency of the ANCF rover model, this computational time is still significantly lower than what was reported in the literature for similar models (Sivo et al., 2019).

3.5 Tractive Force

The tractive forces are examined in this numerical investigation using the two MBS rover models of Section 7.4; the first model consists of 6 brush-type tires, while the second model consists of six ANCF tires. A constant driving moment $M_r = 3.5 \text{ N/m}$ is applied to each wheel for 10 s, in order to have the same dynamic conditions applied to the two tire types. The contact between the rigid ground and the ANCF tires is predicted using a grid of 100 points on the surface of each ANCF plate element. The total tractive force on each ANCF tire is computed as the sum of the tractive forces calculated at each contact point. The dynamic friction coefficient used in the calculation of the tractive forces is $\mu = 0.6$. Figure 25 compares the tractive forces of the front-right wheel obtained with the brush-type and ANCF models. During the first 5 s, the rover reaches equilibrium on the ground and starts accelerating under the effect of the driving moments. It is observed that the ANCF tire, because of its flexibility, captures the oscillatory nature of the tangential friction force which is not captured by the discrete brush-type tire. The oscillations in the ANCF friction forces are due to localized slippage occurring in the contact patch. The use of ANCF tires also allows for capturing high frequency localized oscillations resulting from the tire/soil interaction. Such high frequency oscillations, which cannot be captured using simplified tire models such as the brush-type tire, are important for performing accurate durability; and noise,

vibration and harshness (NVH) investigations.

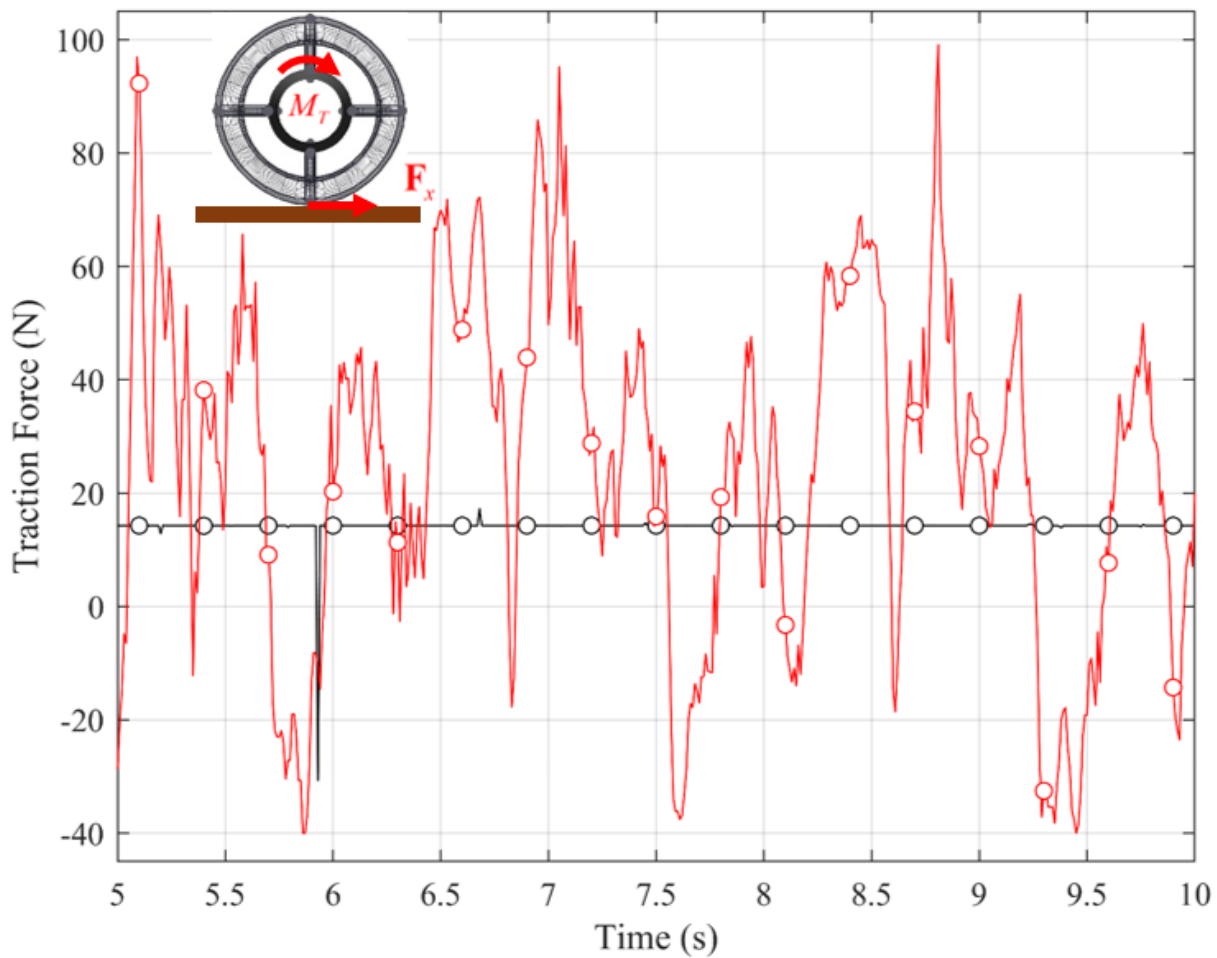


Figure 25. Tractive force

(—●— ANCF airless tire, —●— Brush-type tire)

CHAPTER 4

SUMMARY AND CONCLUSIONS

This thesis describes a geometry/analysis approach for the virtual prototyping of wheeled robots used in the space-exploration missions. Because of the scientific challenges of space explorations, some international space agencies are teaming up together to design autonomous wheeled robots such as the Mars rover considered in this study. The Mars rovers, designed as wheeled robots, collect terrain information, including dust, soil, rocks, and liquids. This thesis describes a computational framework that can be used for both geometry and analysis to avoid the conversion of CAD solid models to analysis meshes and to significantly reduce reliance on physical prototyping which is costly and time-consuming. A computational MBS approach is used to construct and numerically solve the rover differential/algebraic equations. A unified analysis/geometry mesh of the rover *airless wheels*, that can adapt to different soil patterns and harsh operating and environmental conditions without the puncture risk of pneumatic tires, is developed using fully-parameterized ANCF plate elements. The degree of the matrix sparsity in the constrained-dynamics approach used to solve the nonlinear dynamic equations of the MBS rover model is increased by using the ANCF Cholesky coordinates which lead to a generalized identity inertia matrix. Several simulation scenarios are considered, including a drop test and acceleration along a straight line. The numerical results obtained are verified using data published in the literature and are used to evaluate the accuracy and computational efficiency of the ANCF airless-tire modeling approach. The results obtained using the continuum-based ANCF tire model are also compared with the results of the discrete brush-type tire model.

CITED LITERATURE

1. Acary, V., Brémond, M., Kapellos, K., Michalczyk, J., and Pissard-Gibollet, R., 2013, "Mechanical Simulation of the Exomars Rover using Siconos in 3DROV". *12th Symposium on Advanced Space Technologies in Robotics and Automation*, ESA/ESTEC, Noordwijk, Netherlands.
2. Asnani, V., Delap, D., and Creager, C., 2009, "The Development of Wheels for the Lunar Roving Vehicle". *National Aeronautics and Space Administration*, n. 215798.
3. Bauer, R., Barfoot, T., Leung, W., and Ravindran, G., 2008, "Dynamic Simulation Tool Development for Planetary Rovers". *International Journal of Advanced Robotic System*, 5(3), pp. 311 - 314.
4. Bauer, R., Leung, W., and Barfoot, T., 2005, "Development of a Dynamic Simulation Tool for the Exomars Rover". *The 8th International Symposium on Artificial Intelligence, Robotics and Automation in Space (iSAIRAS)*, Munich, Germany.
5. Bauer, R., Leung, W., and Barfoot, T., 2005, "Experimental and Simulation Results of Wheel-Soil Interaction for Planetary Rovers". *Proceedings of IEEE/RSJ international conference on intelligent robots and systems (IROS)*, pp. 586 - 91, Edmonton, Canada.
6. Blundell, M., and Harty, D., 2004, *Multibody Systems Approach to Vehicle Dynamics*, Elsevier, New York.
7. Chottiner, J. E., *Simulation of a Six Wheeled Martian Rover Called the Rocker Bogie*, Master's thesis, The Ohio State University.
8. Ding, L., Deng, Z., Gao, H., Nagatani, K., and Yoshida, K., 2011, "Planetary Rovers' Wheel-Soil Interaction Mechanics: New Challenges and Applications for Wheeled Mobile Robots". *Intel Serv Robotics*, 4, pp. 17 - 38.
9. Ding, L., Gao, H., Deng, Z., and Tao, J., 2011, "Wheel Slip-Sinkage and its Estimation Model of Lunar Rover". *J. Cent. South Univ. Technol*, 17 (1), pp. 129 - 135.
10. Ding, L., Gao, H., Deng, Z., Tao, J., Iagnemma, K., and Liu, G., 2014, "Interaction Mechanics Model for Rigid Driving Wheels of Planetary Rovers Moving on Sandy Terrain with Consideration of Multiple Physical Effects". *J. Field Robot*, 32 (6), pp. 827 - 859.
11. Farin, G., 1999, *Curves and Surfaces for CAGD*, A Practical Guide, Fifth Edition, Morgan Kaufmann, Publishers, San Francisco.
12. Favaedi, Y., and Pechev, A., 2008, "Development of Tractive Performance Prediction for Flexible Wheel". *10th ESA workshop on advanced space technologies for robotics and automation*, Noordwijk, Netherlands.

13. Favaedi, Y., Pechev, A., Scharringhausen, M., et al., 2011, "Prediction of Tractive Response for Flexible Wheels with Application to Planetary Rovers". *J. Terramechanics*, 48 (3), pp. 199 - 213.
14. Fotland, G., Haskins, C., and Rølvåg, T., 2019, "Trade Study to Select Best Alternative for Cable and Pulley Simulation for Cranes on Offshore Vessels". *Systems Engineering*, pp. 1 - 12, DOI: 10.1002/sys.21503.
15. Gajjar, B. I., and Johnson, R. W., 2002, "Kinematic Modeling of Terrain Adapting Wheeled Mobile Robot for Mars Exploration". *Third International Workshop on Robot Motion and Control*, pp. 291 - 296.
16. Gallier, J., 2011, *Geometric Methods and Applications: For Computer Science and Engineering*, Springer, New York.
17. Garrett, S. and Abhinandan, J., 2008, "Wheel-Terrain Contact Modeling in the ROAMS Planetary Rover Simulation". *Proceedings of the ASME 2005 International Design Engineering Technical Conferences and Computers and Information in Engineering Conference*, 6, pp. 89 - 97.
18. Gipser, M., 2005, "FTire: A Physically Based Application-Oriented Tyre Model for Use with Detailed MBS and Finite-Element Suspension Models". *Veh. Syst. Dyn.*, 43(1), pp. 76 - 91.
19. Goetz, A., 1970, *Introduction to Differential Geometry*, Addison Wesley.
20. Grand C., Amar, B., and Bidaud, P., 2001, "A Simulation System for Behavior Evaluation of Off-Road Mobile Robots". *Proceedings of the 4th international conference on climbing and walking robotics*, pp. 307 - 314, Karlsruhe, Germany.
21. Grand, C., Amar, F. B., Plumet F., et al., 2002, "Simulation and Control of High Mobility Rovers for Rough Terrains Exploration". *Proceedings of the IARP international workshop on humanitarian demining*, n.1.
22. Grossi, E., and Shabana, A. A., 2019, "Analysis of High-Frequency ANCF Modes: Navier-Stokes Physical Damping and Implicit Numerical Integration". *Acta Mechanica*, 230(7), pp. 2581 - 2605.
23. Grossi, E., Desai, C. J., and Shabana, A. A., 2019, "Development of Geometrically Accurate Continuum-Based Tire Models for Virtual Testing". *Journal of Computational and Nonlinear Dynamics*, 14, pp. 121006-1 - 121006-11.
24. Hartl, A. E., 2011, *Modeling and Simulation of the Dynamics of Dissipative, Inelastic Spheres with Applications to Planetary Rovers and Gravitational Billiards*, Ph.D. Thesis, North Carolina State University.
25. He, G., Patel, M., and Shabana, A. A., 2017, "Integration of Localized Surface Geometry in Fully Parameterized ANCF Finite Elements". *Comput. Methods Appl. Mech. Eng.*, 313, pp. 966 - 985.

26. Heverly, M., et al., 2013, "Traverse Performance Characterization for the Mars Science Laboratory Rover". *Journal of Field Robotics*, 30(6), pp. 835 - 846.
27. Hu, W., Tian, Q., and Hu, H. Y., 2014, "Dynamics Simulation of the Liquid-Filled Flexible Multibody System via the Absolute Nodal Coordinate Formulation and SPH Method". *Nonlinear Dynamics*, 75, pp. 653 - 671.
28. Iagnemma, K., Senatore, C., Trease, B., Arvidson, R., Bennett, K., Shaw, A., Zhou, F., Van Dyke, L., and Lindemann, R., 2011, "Terramechanics Modeling of Mars Surface Exploration Rovers for Simulation and Parameter Estimation". *ASME International Design Engineering Technical Conference & Computers and Information Engineering Conference*, IDETC/CIE.
29. Ishigami, G., Otsuki, M., Kubota, T., et al., 2011, "Modeling of Flexible and Rigid Wheels for Exploration Rover on Rough Terrain". *Proceedings of the 28th International Symposium on Space Technology and Science*.
30. Jerome, B. J., Kulchitsky, A. V., Duvoy, P., Iagnemma, K., Senatore, C., Arvidson, R. E., and Moored, J., 2015, "Discrete Element Method Simulations of Mars Exploration Rover Wheel Performance". *Journal of Terramechanics*, 62, pp. 31 - 40.
31. Knuth, M. A., Johnson, J. B., Hopkins, M. A., Sullivan, R. J., and Moored, J. M., 2012, "Discrete Element Modeling of a Mars Exploration Rover Wheel in Granular Material". *Journal of Terramechanics*, 49(1), pp. 27 - 36.
32. Krenn, R., Gibbesch, A., and Hirzinger, G., 2006, "Contact Dynamics Simulation of Rover Locomotion". *The 9th International Symposium on Artificial Intelligence, Robotics and Automation in Space (iSAIRAS)*.
33. Kreyszig, E., 1991, *Differential Geometry*, Dover Publications.
34. Kucherenko, V., Bogatchev, A., and Winnendael, M. V., 2004, "Chassis Concepts for the ExoMars Rover". *8th ESA Workshop on Advanced Space Technologies for Robotics and Automation*, "ASTRA 2004", Vol. c, pp. 1 – 8, Noordwijk, The Netherlands.
35. Leite, A. C., and Schäfer, B., 2011, "On Multi-Objective Optimization of Planetary Exploration Rovers Applied to Exomars-type Rovers". *ESA/ESTEC*, Noordwijk, Netherlands.
36. Liu, C., Tian, Q., and Hu, H.Y., 2011, "Dynamics of Large Scale Rigid-Flexible Multibody System Composed of Composite Laminated Plates". *Multibody System Dynamics*, 26, pp. 283 - 305.
37. Loizeau, D., 2015, "ExoMars 2018: The Candidate Landing Sites". *46th Lunar and Planetary Science Conference*, The Woodlands, Texas, USA.
38. Lugner, P., Pacejka, H., and Plöchl, M., 2005, "Recent Advances in Tyre Models and Testing Procedures". *Veh. Syst. Dyn.*, 43(6 - 7), pp. 413 - 426.
39. Ma, C., Wang, R., Wei, C., and Zhao, Y., 2016, "A New Absolute Nodal Coordinate

- Formulation of Solid Element with Continuity Condition and Viscosity Model”. *International Journal of Simulation: Systems, Science and Technology*, 17(21), pp 10.1 - 10.6.
40. Ma, L., Wei, C., and Zhao, Y., 2020, “Modeling and Verification of a RANCF Fluid Element Based on Cubic Rational Bezier Volume”. *ASME Journal of Computational and Nonlinear Dynamics*, 15(4), 041005 1125.
 41. McCoubrey, R., 2014, “Canada’s Suspension and Locomotion Subsystem for ExoMars 2018”. *International Astronautics Congress 2014*, pp. 3 - 6, Toronto, Canada.
 42. Mccoubrey, R., 2014, “ExoMars Suspension and Locomotion”. *iSAIRAS*, pp. 4 - 7, Montreal, Canada.
 43. Nachbagauer, K., 2014, “State of the Art of ANCF Elements Regarding Geometric Description, Interpolation Strategies, Definition of Elastic Forces, Validation and Locking Phenomenon in Comparison with Proposed Beam Finite Elements”. *Archives of Computational Methods in Engineering*, 21(3), pp. 293 - 319.
 44. Nicolini, A., Mocera, F., and Somà, A., 2019, “Multibody simulation of a tracked vehicle with deformable ground contact model”. *Proc IMechE Part K: J Multi-body Dynamics*, 233(1), pp. 152 - 162
 45. Obrezko, L.P., Matikainen, and M.K., Harish, A.B., 2020, “A Finite Element for Soft Tissue Deformation Based on the Absolute Nodal Coordinate Formulation”. *Acta Mechanica*, [https://doi.org/ 10.1007/s00707-019-02607-4](https://doi.org/10.1007/s00707-019-02607-4). [Online; accessed 05/05/2020].
 46. Orzechowski, G., and Fraczek, J., 2015, “Nearly Incompressible Nonlinear Material Models in the Large Deformation Analysis of Beams using ANCF”. *Nonlinear Dynamics*, 82(1), pp. 451 - 464.
 47. Pacejka, H.B., 2006, *Tyre and Vehicle Dynamics*, Second edition, Elsevier, Oxford, England.
 48. Pappalardo, C.M., Biondo, A., Oliva, A., and Guida, D., 2020, “A General Method for Performing an Integrated CAD-MBD-FE Analysis”. *Advanced Manufacturing Processes*, Tonkonogyi, V. et al. (Eds), InterPartner-2019, LNME, Springer, pp. 264 - 272.
 49. Pappalardo, C. M., Wallin, M., and Shabana, A. A., 2017, “A New ANCF/ CRBF Fully Parameterized Plate Finite Element”. *ASME J. Comput. Nonlinear Dyn.*, 12(3), n. 031008.
 50. Patel, M. D., Pappalardo, C. M., Wang, G., and Shabana, A. A., 2019, “Integration of Geometry and Small and Large Deformation Analysis for Vehicle Modelling: Chassis, and Airless and Pneumatic Tyre Flexibility”. *Int. J. Veh. Perform.*, 5(1), pp. 90 - 127.
 51. Patel, M., Orzechowski, G., Tian, Q., and Shabana, A. A., 2016, “A New Multibody System Approach for Tire Modeling Using ANCF Finite Elements”. *Proc. Inst. Mech. Eng., Part K*, 230(1), pp. 69 - 84.
 52. Patel, N., Slade, R., and Clemmet, J., 2010, “The ExoMars Rover Locomotion Subsystem”.

- Journal of Terramechanics*, 47(4), pp. 227 - 242.
53. Perez-Davis, M. E., and Gaier, J. R., 1990, "The Chemical Effects of the Martian Environment on Power System Component Materials: A Theoretical Approach". *NASA Technical Memorandum*, n. 103203.
 54. Petersen, W., and McPhee, J., 2011, "A Study of Volumetric Contact Modelling Approaches in Rigid Tire Simulation for Planetary Rover Application". *International Journal of Vehicle Design*, 64(2 - 4), pp. 262 - 279.
 55. Petersen, W., Vyasarayani, C.P., and McPhee, J., 2011, "Flexible Planetary Rover Tire Model with Volumetric Wheel/soil Interface". *17th International Conference of the International Society for Terrain-Vehicle Systems*, pp. 473 - 480.
 56. Piegl, L., and Tiller, W., 1997, *The NURBS Book*, Second Edition, Springer, Berlin.
 57. Poulakis, P., Vago, J. L., Loizeau, D., Vicente-Arevalo, C., Hutton, A., McCoubrey, R., Arnedo-Rodriguez, J., Smith, J., Boyes, B., Jessen, S., Otero-Rubio, A., Durrant, S., Gould, G., Joudrier, L., Yushtein, Y., Alary, C., Zekri, E., Baglioni, P., Cernusco, A., Maggioni, F., Yague, R., and Ravera, F., 2015, "Overview and Development Status of the ExoMars Rover Mobility Subsystem". *13th ESA Workshop on Advanced Space Technologies for Robotics and Automation*, Noordwijk, The Netherlands.
 58. Rogers, D.F., 2001, *An Introduction to NURBS with Historical Perspective*, Academic Press, San Diego, CA.
 59. Schäfer, B., and Gibbesch, A., 2007, "Planetary Rover Mobility: Wheel-Soil Interaction Based on Multibody System Approach". *IFAC Proc Vol*, 40, pp. 883 - 888.
 60. Scharringhausen, M., Beermann, D., Krömer, O., and Richter, L., 2009, "A Wheel-Soil Interaction Model for Planetary Application". *11th European Regional Conference on Terrain-Vehicle Systems (ISTVS 2009)*, Bremen, Germany.
 61. Schmid, IC., 1995, "Interaction of Vehicle and Terrain Results from 10 Years Research at IKK". *Journal of Terramechanics*, 32(1), pp. 3 - 26.
 62. Shabana, A. A., 2014, "ANCF Reference Node for Multibody System Applications". *IMEchE J. Multibody Dyn.*, 229(1), pp. 109 - 112.
 63. Shabana, A. A., 2015, "ANCF Tire Assembly Model for Multibody System Applications". *ASME J. Comput. Nonlinear Dyn.*, 10(2), pp. 024504
 64. Shabana, A.A., 2018, *Computational Continuum Mechanics*, Third Edition, John Wiley and Sons, Chichester, UK.
 65. Shabana, A.A., 2019, "Integration of Computer-Aided Design and Analysis (I-CAD-A): Application to Multibody Vehicle Systems", *International Journal of Vehicle Performance*, 5, pp. 300 - 327.

66. Shabana, A. A., 2020, *Dynamics of Multibody Systems*, 5th Edition, Cambridge University Press, Cambridge.
67. Shabana, A.A., and Mikkola, A., 2003, "Use of Finite Element Absolute Nodal Coordinate Formulation in Modeling Slope Discontinuity". *ASME Journal of Mechanical Design*, 125(2), pp. 342 - 350.
68. Shabana, A.A., and Zhang, D., "ANCF Curvature Continuity: Application to Soft and Fluid Materials". *Nonlinear Dynamics*, accepted for publication.
69. Shen, Z., Li, P., Liu, C., and Hu, G., 2014, "A Finite Element Beam Model Including Cross-Section Distortion in the Absolute Nodal Coordinate Formulation". *Nonlinear Dynamics*, 77(3), pp. 1019 - 1033.
70. Siddiqi, A., Weck, O., and Iagnemma, K., 2006, "Reconfigurability in Planetary Surface Vehicles: Modelling Approaches and Case Study". *J Brit Interplanet Soc*, 59(1), pp. 450 - 460.
71. Sivo, S., Stio, A., Mocera, F., and Somà, A., 2019, "A Study of a Rover Wheel for Martian Explorations, Based on a Flexible Multibody Approach". *Proc. Inst. Mech. Eng., Part K*, 0(0), pp. 1 - 16.
72. Stéphane, M., Gibbesch, A., Thüer, T., Krebs, A., Lee, C., Despont, B., Schäfer, B., and Slade, R., 2008, "Development of the ExoMars Chassis and Locomotion Subsystem". *The 9th International Symposium on Artificial Intelligence, Robotics and Automation in Space (iSAIRAS)*, ETH Library, Research Collection.
73. Sullivan, R., Anderson, R., Biesiadecki, J., Bond, T., and Stewart, H., 2011, "Cohesions, Friction Angles, and Other Physical Properties of Martian Regolith from Mars Exploration Rover Wheel Trenches and Wheel Scuffs". *Journal of Geophysical Research*, 116, E02006.
74. Vago, J. L., Westall, F., Pasteur Instrument Teams, Landing Site Selection Working Group, and Other Contributors, 2017, "Habitability on Early Mars and the Search for Biosignatures with the ExoMars Rover". *Astrobiology*, 17(6 - 7), pp. 471 - 579.
75. Van Winnendael, M., Baglioni, P., and Vago, J. L., 2005, "Development of the Esa Exomars Rover". *The 8th International Symposium on Artificial Intelligence, Robotics and Automation in Space (iSAIRAS)*, Munich, Germany.
76. Wang, T., 2020, "Two New Triangular Thin Plate/Shell Elements Based on the Absolute Nodal Coordinate Formulation". *Nonlinear Dynamics*. <https://doi.org/10.1007/s11071-019-05448-x>. [Online; accessed 05/05/2020].
77. Wanga, S., Zoua, M., Dangb, Z., Chenb, B., Zhoua, T., and Suc, B., 2019, "Modelling of Flexible Metal Wheels for Planetary Rover on Deformable Terrain". *Thin-Walled Structures*, 141, pp. 97 - 110.
78. Wong, J.Y., 2010, *Terramechanics and Off-Road Vehicle Engineering: Terrain Behaviour, Off-Road Vehicle Performance and Design*, Elsevier, Amsterdam, The Netherlands.

79. Young, A. H., 2007, *Lunar and Planetary Rovers – The Wheels of Apollo and the Quest for Mars*, Springer, Praxis Publishing Chichester.
80. Zhou, F., Arvidson, R. E., Bennett, K., Trease, B., Lindemann, R., Bellutta, P., Iagnemma, K., and Senatore, C., 2013, “Simulations of Mars Rover Traverses”. *Journal of Field Robotics*, 31(1), pp. 141 - 160.

VITA

NAME Edoardo Samarini

EDUCATION

Master of Science in “Mechanical Engineering”, University of Illinois at Chicago, July 2020, USA

Specialization Degree in “Mechanical Engineering”, July 2020, Polytechnic of Turin, Italy

Bachelor’s Degree in Mechanical Engineering, September 2018, Polytechnic of Turin, Italy

LANGUAGE SKILLS

Italian Native speaker

English Full working proficiency
A.Y. 2019/20 One Year of study abroad in Chicago, Illinois
A.Y. 2018/19. Lessons and exams attended exclusively in English

SCHOLARSHIPS

Summer 2020 Teaching Assistantship (TA) position (20 hours/week) with full tuition waiver plus monthly stipend

Spring 2020 Italian scholarship for final project (thesis) at UIC

CONTACTS

E-mail edoardo.samarini@gmail.com

Linkedin <https://www.linkedin.com/in/edoardo-samarini-85415018b/>